

# **Seasonal Prediction with Neural GCM and Simplified Boundary Forcings: Large-scale Atmospheric Variability and Tropical Cyclone Activity**

Gan Zhang<sup>1\*</sup>, Megha Rao<sup>1</sup>, Janni Yuval<sup>2</sup>, Ming Zhao<sup>3</sup>

<sup>1</sup> Department of Climate, Meteorology, and Atmospheric Sciences, University of Illinois at Urbana-Champaign

<sup>2</sup> Google Research

<sup>3</sup> Geophysical Fluid Dynamics Laboratory, National Oceanic and Atmospheric Administration

\*Corresponding Author: Gan Zhang ([gzhang13@illinois.edu](mailto:gzhang13@illinois.edu))

## Key Points

- NeuralGCM, a hybrid ML-physics model, achieves seasonal predictions of atmosphere and TCs using simplified boundary condition forcing.
- Experiments shows prediction skill for tropical atmospheric variability and TC metrics, notably in North Atlantic and East Pacific.
- Establishes a performance baseline for developing efficient ML seasonal forecasting and seamless weather-climate prediction systems.

## Abstract

Machine learning (ML) models are successful with weather forecasting and have shown progress in climate simulations, yet leveraging them for useful climate predictions needs exploration. Here we show this feasibility using NeuralGCM, a hybrid ML-physics atmospheric model, for seasonal predictions of large-scale atmospheric variability and Northern Hemisphere tropical cyclone (TC) activity. Inspired by physical model studies, we simplify boundary conditions, assuming sea surface temperature (SST) and sea ice follow their climatological cycle but persist anomalies present at initialization. With such forcings, NeuralGCM simulates realistic atmospheric circulation and TC climatology patterns. Furthermore, this configuration yields useful seasonal predictions (July–November) for the tropical atmosphere and various TC activity metrics. Notably, the prediction skill for TC frequency in the North Atlantic and East Pacific basins is comparable to existing physical GCMs. These findings highlight the promise of leveraging ML models with physical insights to model TC risks and deliver seamless weather-climate predictions.

## Plain Language Summary

Scientists are exploring how artificial intelligence (AI) can improve weather and climate predictions. We tested a new computer model, NeuralGCM, which blends AI with established physical equations, to forecast atmospheric states during the Northern Hemisphere hurricane season (July–November). Instead of using complex ocean models, we gave our model a simplified starting point, assuming initial anomalies of ocean temperature and sea ice persist alongside the normal seasonal cycle. Running test forecasts for 1990–2023, we found our model realistically simulated typical atmospheric patterns and tropical cyclone behavior (where/when/how many) even with the simplified input. Importantly, it also showed useful skill in predicting year-to-year variations, forecasting whether hurricane seasons in the Atlantic or East Pacific would be more or less active than average. The prediction skill is comparable to some conventional, computationally intensive models. This research suggests these new AI tools, even with simpler setups, hold promise for improving long-range forecasts of risks like hurricanes. Because they run much faster and simulate many features of interest at the same time, they could lead to more affordable and efficient prediction systems that help communities better prepare for high-impact weather.

Keywords: Subseasonal-to-Seasonal Prediction, Machine Learning, Tropical Cyclone, Model Evaluation.

## 1. Introduction

Machine learning (ML) models recently made breakthroughs in weather forecasting (e.g., Keisler, 2022; Bi et al., 2023; Pathak et al., 2022; Lam et al., 2023; Price et al., 2023; Kochkov et al., 2024). Trained with atmospheric reanalysis or physical model data, these ML models delivered successful forecasts up to two weeks of lead time with skills comparable to or better than conventional numeric weather forecast (NWP) models. With computational costs at a fraction of NWP models ( $10^{-3}$  to  $10^{-5}$ ), the new ML models unlocked opportunities for improving operational weather service (e.g., Lang et al., 2024) and advancing fundamental understanding of atmospheric predictability (e.g., Vonich & Hakim, 2024). Similar to the early development of NWP and climate models (Phillips, 1956), the success of ML models in weather forecasting also inspired researchers to explore their potential applications in climate modeling. Nonetheless, the feasibility of conducting successful climate simulations and society-relevant climate predictions with the new ML models remains to be explored.

Recent efforts in leveraging the new ML models for climate simulations focused on attaining stable long-term simulations and emulating atmosphere-ocean interactions. For example, Cresswell-Clay et al. (2024) trained ML emulators for the atmosphere and the surface ocean separately and showed that linking the two emulators can generate stable atmospheric simulations of the current climate for over 1000 years. Other endeavors emphasized achieving stable long-term simulations by incorporating various physical constraints. Bonev et al. (2023) achieved one-year stable rollouts with the Fourier neural operator (FNO) by replacing an unrealistic flat geometry with spheric geometries. Based on the spheric FNO, Wang et al. (2024) used gridded atmosphere and ocean data to train separate emulators and link them during roll-outs. With a configuration of lagged ensemble forecasting, their linked emulators achieved skillful seasonal predictions of the El Niño–Southern Oscillation (ENSO). Watt-Meyer et al. (2024) introduced mass and moisture constraints to the spheric FNO framework and completed an 80-year historical simulation with realistic atmospheric variability. This set of simulations performed well with in-sample climate forcings but showed unrealistic responses to out-of-sample climate forcings (i.e., zero-shot learning), such as high levels of sea surface temperature (SST) and carbon dioxide. To overcome such limitations, Beucler et al. (2024) proposed to incorporate the physical knowledge of subgrid

processes, which helped ML emulators trained with physical model outputs better generalize across climate regimes.

Distinct from those ML emulators, Kochkov et al. (2024) developed an ML-physics hybrid model (NeuralGCM) and achieved multi-decade, stable atmospheric simulations. This model contains an atmospheric dynamical core like the conventional GCMs but replaces the parameterized subgrid physics with ML substitutes. Compared to the existing ML climate emulators, NeuralGCM stands out with its structural similarity to the conventional NWP models and atmospheric GCMs that are grounded on physical principles. NeuralGCM is highly skillful for weather forecasting and can incorporate observed SSTs to simulate climate anomalies, such as simulating realistic tracks and numbers of TCs in the active 2020 Atlantic hurricane season (Kochkov et al., 2024). These traits make NeuralGCM a promising candidate for modeling extreme risks and developing a seamless weather-climate prediction system (Brunet et al., 2010; Hoskins, 2013), provided that NeuralGCM can be configured to deliver skillful climate predictions.

While the current version of NeuralGCM lacks the means to simulate boundary conditions (e.g., ocean and sea ice) and the support for the atmosphere-ocean coupling, previous studies with physical models suggest that simple assumptions of boundary forcings can help establish a performance baseline for atmospheric GCMs in seasonal prediction tasks. Specifically, Zhao et al. (2010) showed that assuming persistent sea surface temperature (SST) anomalies with a climatological seasonal cycle can help an atmospheric GCM skillfully predict tropical cyclone (TC) activity in the North Atlantic and the Northeastern Pacific. Chen & Lin (2013) suggested that the prediction skill improves when the atmospheric GCM is initialized with observed conditions instead of random conditions from climate simulations. The success of these early studies with physical models builds on the thermal inertia of the tropical ocean and the strong influences of tropical SST on the global atmosphere (e.g., Shukla, 1998) and TC activity (e.g., Gray, 1984). The exploratory work with atmospheric GCMs served as a stepping stone for the ensuing development of more advanced prediction systems (e.g., Delworth et al., 2020; Vecchi et al., 2014).

Inspired by the recent NeuralGCM development and the previous physical studies, this study explores the feasibility of leveraging NeuralGCM to deliver skillful seasonal climate prediction. We emphasize TC activity since these storms are a leading contributor to life losses and economic

damages (World Meteorological Organization, 2021) and often remain challenging for physical GCMs to simulate (Roberts et al., 2020). This TC focus also helps us leverage proven concepts and knowledge in physical model development (Chen & Lin, 2013; Zhao et al., 2010). Overall, this effort establishes a performance baseline for future model development that seeks to extend our climate modeling capability and deliver societally valuable predictions (Emanuel et al., 2012; Lemoine & Kapnick, 2024).

## 2. Data and Methods

### 2.1 Observational Data

The fifth-generation ECMWF atmospheric reanalysis (ERA5) (Hersbach et al., 2020) serves as the primary data for the training, configuration, and validation of NeuralGCM simulations. The gridded ERA5 is generated by a numeric weather forecast model that follows physical laws and ingests multi-sourced observational data (e.g., weather station and satellite data). The original grid spacing of ERA5 is approximately 0.25-degree and contains variables at pressure levels and the surface (e.g., SST and sea ice coverage). The ERA5 data from 1979–2017 and 1979–2019 is used to train the deterministic and the stochastic NeuralGCM, respectively (Kochkov et al., 2024). Since the training is based on narrow time windows ( $\leq 5$  days), NeuralGCM does not directly learn the seasonal evolution trajectories. To facilitate the configuration and validation of retrospective prediction experiments, we regrid the ERA5 data to match the grid of NeuralGCM. While many recent ML studies use TC tracks extracted from the ERA5 for model evaluation, we evaluate TC predictions using the International Best Track Archive for Climate Stewardship (IBTrACS) (Knapp et al., 2010). This dataset includes a collection of hurricane information based on multi-sourced observations and expert quality control. The best track dataset is widely used in TC research and real-world risk modeling and is generally considered more trustworthy than the reanalysis datasets (e.g., ERA5) that struggle with representing intense hurricanes (Dulac et al., 2024).

### 2.2 NeuralGCM Hindcast Experiment

We use the 1.4-degree version of NeuralGCM to balance the need to conduct ensemble predictions and simulate realistic TC activity. At this resolution, NeuralGCM has two models: a deterministic model and a stochastic model. The deterministic model was extensively evaluated

and showed promise in simulating realistic TC activity in the test of the year 2020 (Kochkov et al., 2024). The stochastic configuration uses random seeds to generate space-time correlated Gaussian random fields for perturbing initial conditions and insert stochasticity into the neural network parameterization. These random fields are independent of each other and conceptually resemble the NWP techniques of perturbing the initial fields and the parameterized model physics Kochkov et al. (2024). Additional descriptions of this stochastic version are available in the supplementary materials of Kochkov et al. (2024). We conduct hindcast experiments using both configurations to assess the potential sensitivity of TC activity to the learned model physics parameters. To generate ensemble predictions with the deterministic model, we introduce perturbations to the initial conditions using a Gaussian random field. This field, initialized from a random seed, is applied to the learned correction within the NeuralGCM's encoder. Specifically, the encoder interpolates ERA5 initial conditions to sigma levels and subsequently learns a correction to this interpolation. We then perturb this correction by multiplying it by a factor of  $(1+\text{random\_field\_value})$ , where `random_field_value` represents the value from the generated Gaussian random field with correlation length of 1000 km for the deterministic model. We use this perturbation strategy to initialize twenty-member ensemble simulations at 0 UTC on July 1 for each year from 1990 to 2023. We also generated additional simulations (e.g., 1979–1989) to facilitate comparisons with previous TC studies that used physical models (Supplementary Materials).

Inspired by the seasonal prediction experiments by Zhao et al. (2010) and Chen & Lin (2013), we use the climatological seasonal cycle and persistent anomalies of SST and sea ice to drive the NeuralGCM. Based on the autocorrelation of SST and sea ice, this configuration can approximate the evolution of tropical SST (Chen & Lin, 2013) and sea ice (Bushuk et al., 2022) during July–November. When calculating the anomalies of SST and sea ice at the initialized time, we use the daily climatology of 1991–2020 that is resampled using the monthly data. To ensure the consistency among variables and the configurations described by Kochkov et al. (2024), the initial states of the SST, sea ice, and atmosphere are acquired from the ERA5. At later steps of the prediction experiment, we force NeuralGCM with the pre-calculated SST and sea ice fields, namely the sum of their daily climate values and anomalies at the initialization time. Therefore, all the information needed for long-range predictions is available near the initialization time. We run the predictions for approximately five months to cover much of the TC season of the Northern

Hemisphere. We acknowledge the assumption of persistent anomalies has limitations and consider the prediction skill of our experiments as a lower bound on the attainable skills.

### 2.3 Post-Processing and Evaluation

The combination of the stochastic NeuralGCM and modified boundary conditions yields stable multi-month predictions in most cases. While the hindcasts with the deterministic physics are generally stable (~98.5%), about 10% of the simulations with the stochastic physics configuration show spurious small-scale waves (Supplementary Figures 1 and 2) associated with unrealistic convection and stratosphere features. These waves mostly appear in the tropics and violate the weak gradient constraint of the real-world atmosphere (Charney, 1963; Sobel & Bretherton, 2000). While fixes are being explored, this study proceeds by labeling the simulations with spurious waves using a check of tropical variability. Specifically, we calculate the standard deviations of 500-hPa geopotential height in the zonal direction and compare the metric between the initial and later prediction steps. If spurious small-scale waves develop, they will substantially increase the zonal variability and thus the instability metric. If this metric exceeds two times the initial metric values at any latitudes during the roll-outs, we flag the corresponding simulation as unstable and assign all the fields to climate values. The flagging is robust to small changes in the threshold as the spurious waves usually amplify quickly once appearing in the rollouts. As the Supplementary Materials will show, the skills of the deterministic and the stochastic hindcasts in predicting TC activity are comparable. Unless otherwise specified, the analyses and discussion in the main text focus on the hindcasts with the more stable configuration with deterministic model physics.

The prediction evaluation includes selected environmental variables and metrics of TC activity. The dynamical variables include the 500-hPa geopotential height, which characterizes the steering flow that affects TC tracks, and the 200-850 hPa vertical wind shear, which affects TC genesis and development. While evaluating convection-related variables is important, the NeuralGCM version used here does not include precipitation variables. A new version that can simulate realistic precipitation is under development (Yuval et al., 2024). We apply the TempestExtreme package (Ullrich et al., 2021) to track TCs in our retrospective prediction experiments. The tracking uses the vorticity-based method and does not impose any wind speed thresholds. We follow most parameter choices of the TC tracker used by Kochkov et al. (2024) who tuned the parameters such that the TC counts of the ERA5 at 0.25-degree resolution match

the values at 1.4 degrees. To better match the TC counts in the IBTrACS, we lower the vorticity threshold to  $4 \times 10^{-5} \text{ s}^{-1}$  and set the storm duration threshold to 54 hours. Following previous studies of TC activity (e.g., Chen & Lin, 2013; Zhang et al., 2021; Zhao et al., 2010), we mainly evaluate the ensemble mean and examine the metrics of anomaly correlation coefficient and root-mean-squared error. We also provide results from other models (e.g., Chen & Lin, 2013, Johnson et al. 2019; Zhang et al. 2019) for reference but refrain from pursuing more comprehensive comparisons considering data availability and other issues (Supplementary Materials).

### 3. Results

#### 3. 1 Model Skill with Large-scale Atmospheric Environment

The NeuralGCM hindcasts with simplified boundary forcings simulate the atmospheric climate and seasonal cycle realistically (Figure 1). The July-November means of the 500-hPa geopotential height of the NeuralGCM and the ERA5 show consistent climate patterns. Their differences are the smallest in the tropics and the largest in the Arctic region. An inspection of the seasonal evolution of the zonal means of the 500-hPa geopotential height suggests the model biases grow over time. The initial biases emerge in the polar region and develop relatively rapidly during the transition season. The biases in the tropics are relatively small and comparable to those in a fully coupled physical prediction system (Supplementary Figure 3). Preliminary analyses (not shown) suggest that the high-latitude biases are related to the simplified boundary forcings, especially the ice representation in polar regions. The seasonally evolving geopotential biases affect the midlatitude jet streams and may ultimately distort some aspects of the tropical-extratropical teleconnections and TC activity (Wang et al., 2020; Zhang et al., 2016). Comparing other atmospheric variables suggests similar evolution between the climate states of the NeuralGCM and the ERA5 (not shown). Similar biases and consistency are present in the hindcasts with the stochastic version of NeuralGCM (not shown). Their overall consistency between the model climate and the observation is notable considering the simplified boundary forcings and the lack of complex atmosphere-land-ocean coupling in the NeuralGCM hindcasts.

The NeuralGCM hindcasts also show skills in predicting year-to-year variability of the monthly mean atmospheric environment. We examine variables including the 500-hPa geopotential, surface pressure, 1000-hPa temperature, and vertical shear of zonal wind (200-850

hPa) and find that the NeuralGCM hindcasts show various skill levels across the examined month leads (Supplementary Figures 4-11). Preliminary comparisons between the NeuralGCM hindcasts (Supplementary Figures 4-11) and operational seasonal predictions by a fully coupled physical model (Johnson et al. 2019; Supplementary Figures 12-14) suggests the anomaly correlation coefficients with the observation are overall lower for the NeuralGCM hindcasts with simplified boundary forcings. Nonetheless, the anomaly correlation coefficients for NeuralGCM hindcasts show spatial-temporal patterns similar to those of the physical model. The anomaly correlation coefficients of the initial month are the highest and decrease with forecast lead time. While the decay quickly makes extratropical predictions unskillful, the prediction skill persists at much longer forecast lead in the tropics, as suggested by the relatively high correlation coefficients and low prediction errors (Supplementary Figures 4-11). The relatively high skill in the tropics corresponds to regions where the SST strongly regulates atmospheric variability (Shukla, 1998), consistent with similar experiments with physical GCMs (Chen & Lin, 2013).

We next focus on the prediction of the atmospheric environment in the Main Development Regions (MDRs). The MDRs, as outlined in Figure 1c, span over 10°N–25°N of the tropical oceans and contribute most TCs that form in the Northern Hemisphere. Figure 2 shows the skill of the NeuralGCM with simplified boundary forcings in predicting the MDR atmospheric environment. The predictions of near-surface air temperature and the 500-hPa geopotential show the highest anomaly correlation coefficients with the observation across the three examined MDRs. For the prediction of these two variables, the anomaly correlation coefficients are statistically significant for each calendar month (Figure 2a–c). In comparison, the anomaly correlation coefficients for the surface pressure and the zonal wind shear are much lower but can remain statistically significant in August (Lead Days = 31-62). The anomaly correlation coefficients generally exceed those of persisting the monthly anomalies of June (Supplementary Figure 15). The findings thus suggest that the NeuralGCM with simplified boundary forcings can predict some aspects of the large-scale atmospheric variability in the MDRs. Such skills in predicting the large-scale environment are essential for the subseasonal-to-seasonal predictions of TC activity.

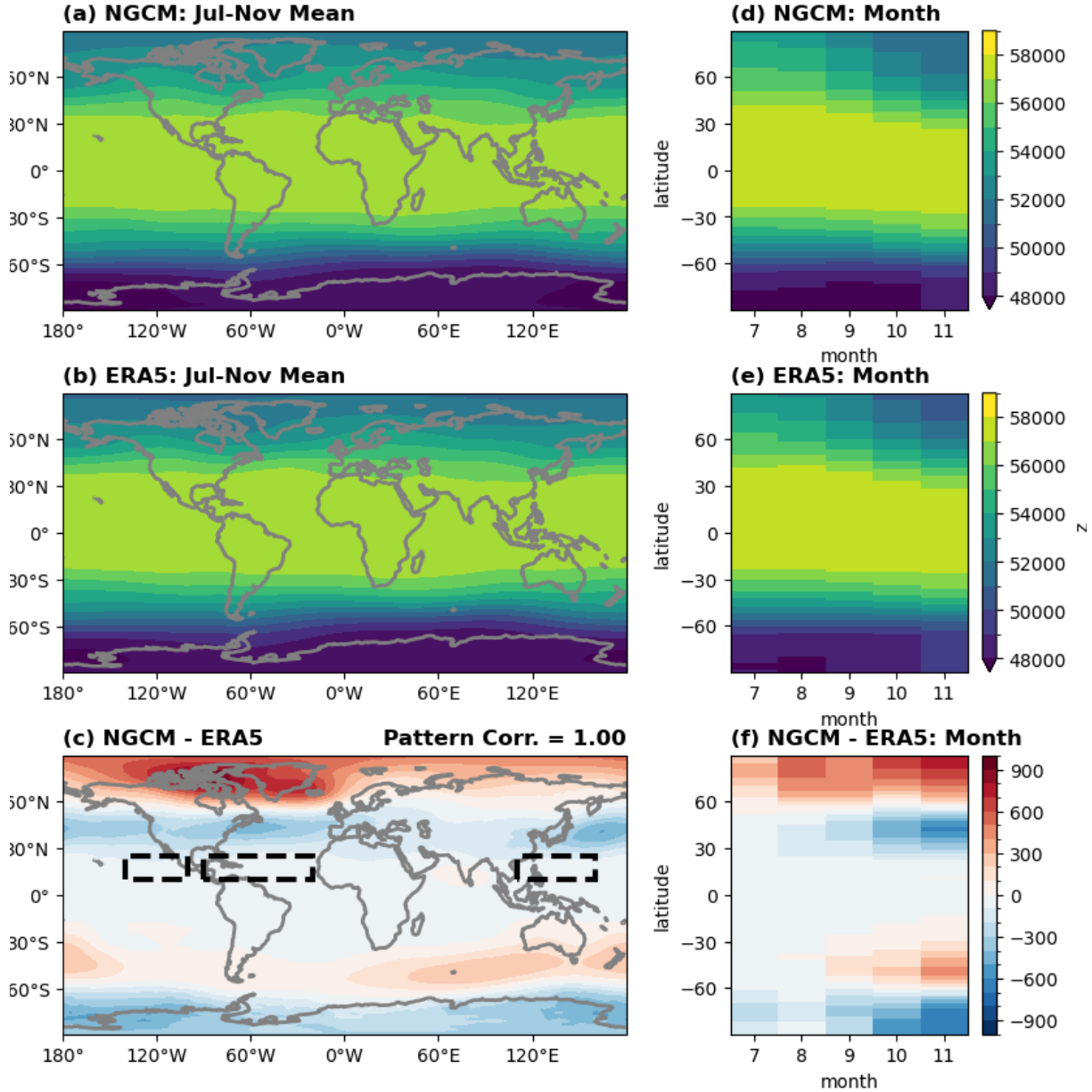


*Figure 1 Comparison of the large-scale atmospheric environment in NeuralGCM hindcasts and the ERA5. (a) July-November ensemble mean (1990-2019) of the 500-hPa geopotential ( $m^2 s^{-2}$ ) in the NeuralGCM hindcasts. (b) Same as (a), but for the ERA5. (c) The difference between (a) the NeuralGCM hindcasts and (b) the ERA5. The pattern correlation (rounded to 2 decimal places) between (a) and (b) is denoted in the top right corner of (c). (d) The monthly evolution of the zonal mean of the 500-hPa geopotential ( $m^2 s^{-2}$ ) in the NeuralGCM hindcasts. (e) Same as (d), but for the ERA5. (f) The difference between (d) the NeuralGCM hindcasts and (e) the ERA5. The dashed black lines in (c) highlight the regions where the environmental prediction skill is evaluated.*

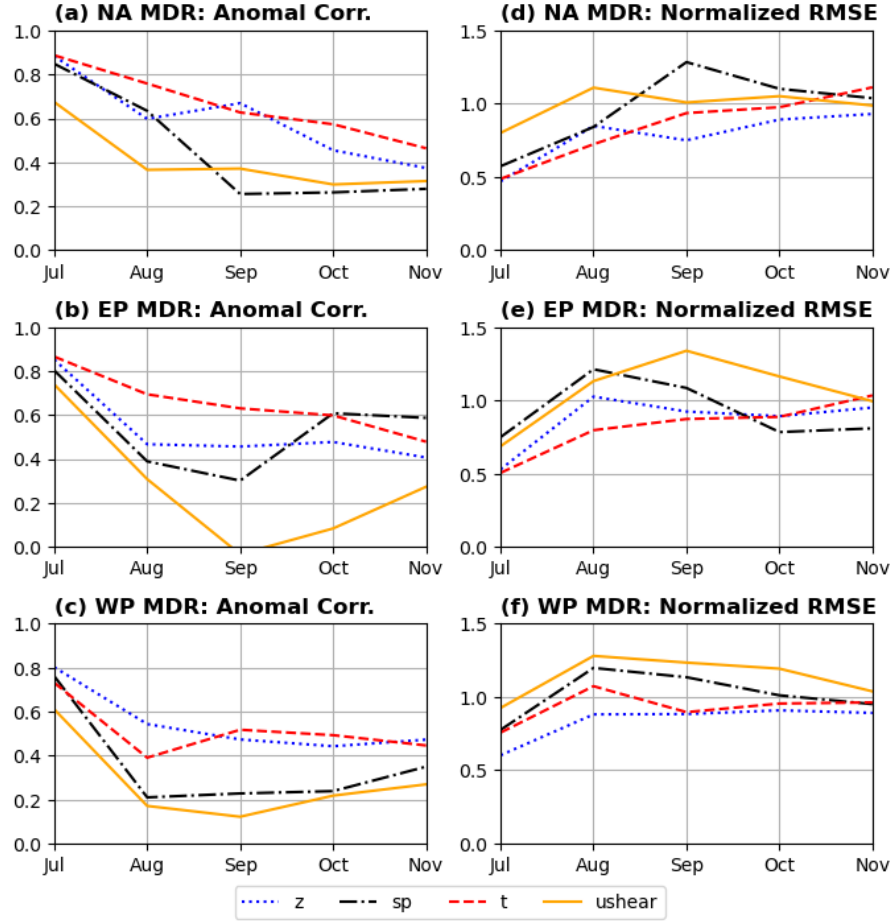


*Figure 2 Prediction skills of NeuralGCM for the Main Development Regions (MDRs) of TCs. The plot shows selected atmospheric variables, including the 500-hPa geopotential ( $z$ ), surface pressure ( $sp$ ), 1000-hPa temperature ( $t$ ), and vertical shear of zonal wind (200-850 hPa) ( $ushear$ ). (a) The anomaly correlation coefficient of the MDR in the North Atlantic (NA). (b) Same as (a), but for the Northeast Pacific (EP). (c) Same as (a), but for the Northwest Pacific (WP). (d, e, f) Same as (a, b, c), but for the normalized root-mean-squared error. The scaling factor is the year-to-year standard deviations of the ERA5 data. The skill metrics are calculated using data from 1990-2023 for each grid point and then averaged over the MDR domains highlighted in Figure 1c. The 95% confidence threshold for the anomaly correlation coefficient is  $\sim 0.28$ .*

### 3.2 Model Skill with TC Activity

The NeuralGCM hindcast can simulate a realistic spatial-temporal distribution of TC activity (Figure 3). The kernel density estimation of the simulated and observed TC activity shows consistent spatial patterns, including the high density of TC tracks in parts of the Northeast Pacific and the Northwest Pacific (Figures 3a-c). The relative track density among the Northern Hemisphere basins is also realistic, free of the common bias of many physical GCMs in severely underestimating TC activity in the Northern Hemisphere (e.g., Roberts et al. 2020). The seasonal cycles of TC activity in the Neural GCM and the observation are also similar (Figures 3d and 3e). The similarities include the latitudinal shift towards lower latitudes in the late season and the high concentration (~75%) of samples in July-September. The comparisons also show subtle biases of the NeuralGCM hindcasts with deterministic physics. For instance, the kernel density of TC tracks is too high near 10–20°N in the Northeast Pacific; the decay of TC activity in the late season is also too fast, with October–November accounting for 17% instead of 25% of tracks. Similar seasonality biases are present in the NeuralGCM hindcasts with stochastic physics (not shown). This suggests these biases might arise from the simplified boundary forcings and biases in simulating the large-scale environment (Figure 1f), though the parameter choice of tracking algorithms may also be a contributing factor.

The NeuralGCM hindcast also simulates interannual variations of TC activity that are significantly correlated with the observation. The correlations between the seasonal prediction and the observation of the basin-wide TC frequency are statistically significant in the North Atlantic and the Northeast Pacific (Figure 4). Despite the low model resolution and computational costs of the NeuralGCM hindcasts, its skill is comparable to previous physical model simulations with similar simplified boundary forcings (Chen & Lin, 2013; Zhao et al., 2010) or a more realistic representation of boundary forcings (e.g., Zhang et al., 2019) (Supplementary Table 1). Focusing on individual years, the NeuralGCM hindcast manages to predict some hyper-active seasons (e.g., the 2005 North Atlantic season). Encouragingly, the prediction of the 2018–2023 seasons, which is not used to train the deterministic model, also shows some skill in the North Atlantic and the Northeast Pacific (Figures 4a and 4b). Although the prediction of TC frequency in the Northwest Pacific and the North Indian Ocean is weakly correlated with the observation (Figures 4c and 4d), the NeuralGCM hindcast shows skills in predicting other aspects of TC activity in the Northwest

Pacific. For example, the predicted track density in open-ocean areas of the Northwest Pacific is significantly correlated with the observation (Supplementary Figure 16a). Similar basin-wide and regional correlations are identified using the NeuralGCM hindcasts with the stochastic configuration (Supplementary Figures 16b and 17). The regions with high prediction skills are consistent with physical model simulations and predictability analysis (Zhang et al. 2019).

Interestingly, the NeuralGCM hindcast and the observation show significant correlations in intensity-related TC activity metrics, such as the accumulated cyclone energy (ACE). For the experiments with deterministic physics, we identified statistically significant correlations for the North Atlantic ( $r = 0.68$ ), the Northeast Pacific ( $r = 0.59$ ), and the Northwest Pacific ( $r = 0.42$ ) (Supplementary Figure 18). The hindcast with the stochastic physics shows comparable or better skill in predicting the ACE of the North Atlantic ( $r = 0.73$ ), the Northeast Pacific ( $r = 0.56$ ), and the Northwest Pacific ( $r = 0.53$ ) (Supplementary Figure 19). We also compared the skill of these hindcast experiments and a physical model with a higher spatial resolution (Zhang et al. 2019). During the 1981-2014 period, the NeuralGCM hindcasts and the physical model have comparable anomaly correlation coefficients in predicting the ACE in the North Atlantic, but the skill of the NeuralGCM hindcasts is notably lower with the Northeast and Northwest Pacific (not shown). The skill difference in predicting the ACE is possibly attributable to regional model biases and difficulties of the NeuralGCM hindcasts in representing intense TCs ( $>60 \text{ m s}^{-1}$ ) (Supplementary Figure 20). Nonetheless, this intensity-related issue is expected considering the lower resolution of the NeuralGCM (1.4-degree vs  $\sim 0.5$ -degree) used to generate our hindcasts.

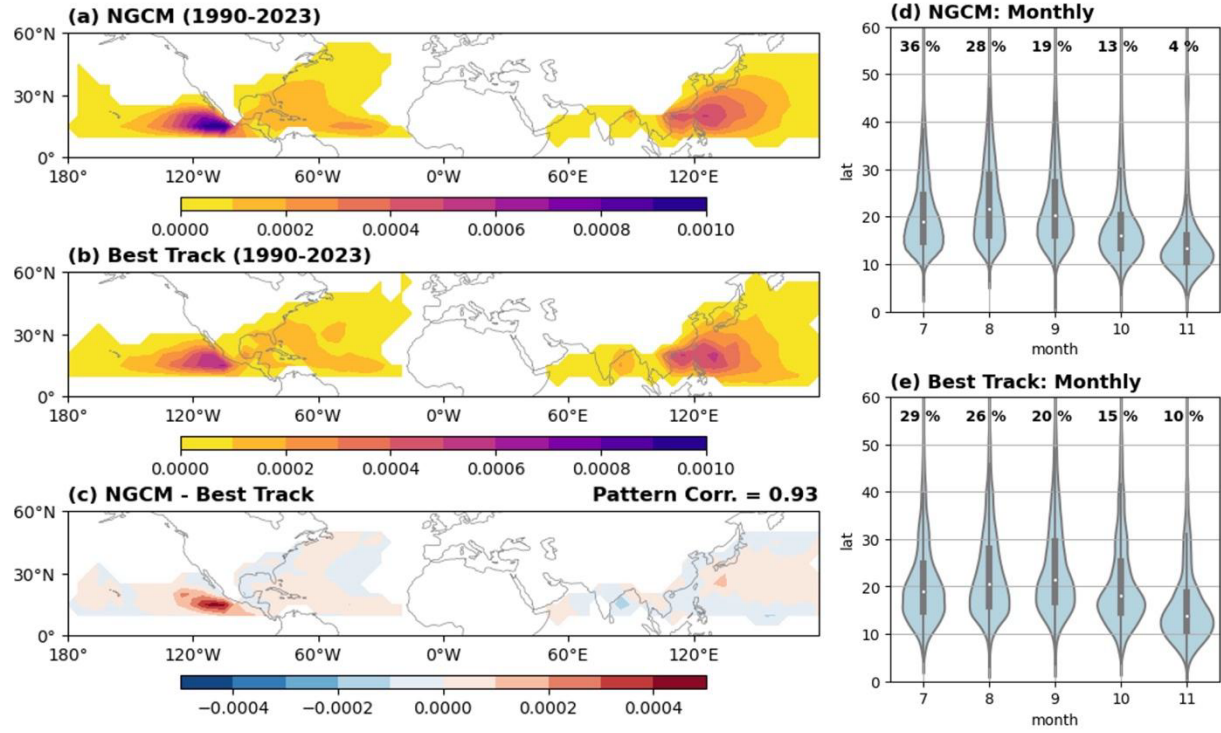


*Figure 3 Comparison of July-November TC activity in NeuralGCM hindcasts and the IBTrACS (1990-2023). (a) Kernel density of the TCs identified in the NeuralGCM hindcasts. (b) Same as (a), but for the best track observations. (c) The difference between (a) the NeuralGCM hindcasts and (b) the IBTrACS. The pattern correlation between (a) and (b) is denoted in the top right corner of (c). (d) The monthly evolution of the latitudinal distributions of the Northern Hemisphere TCs in the NeuralGCM hindcasts. The miniature box-and-whisker plots show the median, the interquartile range (IQR), and the  $1.5 \times \text{IQR}$  range. The monthly percentage of the track points in the July-November total is denoted in the upper part. (e) Same as (d), but for the best track.*

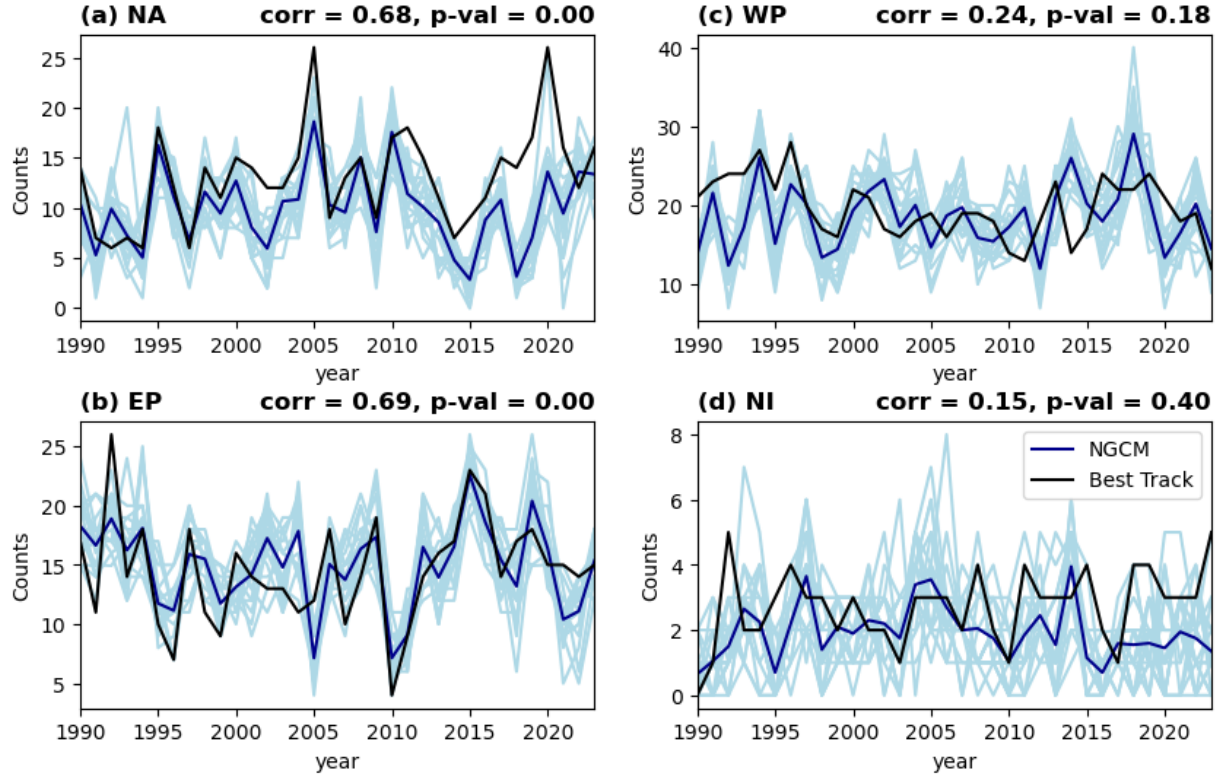


*Figure 4 Predictions and observations of the basin-wide TC counts (1990-2023). (a) North Atlantic, (b) Northwest Pacific, (c) Northeast Pacific, and (d) North Indian Ocean. The black line shows the annual hurricane counts in the observation. The blue lines show the counts in the NeuralGCM hindcasts. The dark blue line shows the ensemble mean, and the light blue line shows the individual ensemble members. The correlations between the ensemble means and the observation, as well as the associated statistical significance, are denoted in the top right corner of each subplot and summarized in Supplementary Table 1.*

## 4. Summary and Discussion

This study conducts experimental seasonal predictions with the newly available NeuralGCM and simplified boundary forcings. Inspired by earlier studies with physical GCMs, the hindcast experiments focus on July to November which account for most TC activity in the Northern Hemisphere. The NeuralGCM hindcasts can simulate realistic climate states of the atmosphere environment and TC activity. When predicting atmospheric variability, the NeuralGCM hindcast

shows statistically significant anomaly correlation coefficients with the ERA5 reference at various forecast leads. Consistent with experiments conducted with physical GCMs, the skills are the highest for the environmental variables in the tropics. The hindcast also achieves relatively high skills in predicting seasonal metrics of TC activity, notably in the North Atlantic and the Northeast Pacific. For instance, the prediction skill of TC activity metrics such as basin-wide TC frequency is comparable to physical models with much higher spatial resolution (e.g., Chen and Lin 2013) or more complex coupled processes (e.g., Zhang et al. 2019) (Supplementary Table 1). The skill with this physics-ML model is encouraging considering the simplified nature of boundary forcings and the low computational costs.

This study has several caveats related to the comparison with operational prediction models and the simplified boundary forcings. Since the TC data of most operational climate prediction models are not publicly accessible, we were unable to comprehensively compare our results with state-of-the-art models and evaluate potential differences (Supplementary Materials). The simplified boundary forcings used in this study rely on the persistence of anomalies and can be less reasonable for other initialization time. We speculate that more realistic representations of boundary forcings or the inclusion of coupled climate processes (e.g., land-atmosphere coupling) may help NeuralGCM to accomplish more skillful predictions of TC activity (e.g., Zhang et al., 2021) and other aspects of the Earth system (e.g., Yeager et al., 2018). Such development can be accomplished by coupling NeuralGCM with statistical models, ML emulators, or other hybrid models of the ocean and other Earth system components.

Contributing to the rapidly evolving field of the ML-based climate modeling, this study demonstrates a practical application of the NeuralGCM and provides valuable insights for future model development. Our hindcast experiments with simplified boundary forcings shows that the NeuralGCM can represent the atmospheric responses to boundary forcings (e.g., SST) that are critical for the subseasonal-to-seasonal prediction. These experiments establish a performance baseline against which future model iterations can be benchmarked. Furthermore, our results suggest that the NeuralGCM holds significant potential as a foundation for developing a computationally affordable system for seamless subseasonal-to-seasonal prediction. Nevertheless, the evaluation also underscores some challenges of applying the current ML atmospheric models, including limitations inherited from training datasets and the lack of coupling

among key climate system components. Recognizing that physical GCMs required decades of refinement to achieve milestones like simulating realistic TC activity (Manabe et al., 1970; Roberts et al., 2020; Zhao et al., 2009), patience and continued effort are warranted despite recent breakthroughs in ML modeling efforts. We expect intensified collaboration among ML and physical science communities to alleviate many of the identified issues, ultimately accelerating the transformation of climate model development and applications.

## Acknowledgment

G.Z is supported by the faculty development fund of the University of Illinois at Urbana-Champaign, and the faculty fellowship of the Office of Risk Management and Insurance Research (ORMIR) of Gies Business School, and the U.S. National Science Foundation award AGS-2327959. The authors thank Sarah Henry and Zhuo Wang for stimulating discussions about refining the NeuralGCM simulations. GZ thanks the organizers of the Rossbypalooza workshop at the University of Chicago for providing a welcoming environment for attendees.

## Code and Data Availability

The NeuralGCM code is available at GitHub (<https://github.com/google-research/neuralgcm>) under the Apache 2.0 license. The data and code used to generate the plots in this study will be available at a Zenodo repository before publication.

## References

Beucler, T., Gentine, P., Yuval, J., Gupta, A., Peng, L., Lin, J., et al. (2024). Climate-invariant machine learning. *Science Advances*, 10(6), eadj7250.  
<https://doi.org/10.1126/sciadv.adj7250>

Bi, K., Xie, L., Zhang, H., Chen, X., Gu, X., & Tian, Q. (2023). Accurate medium-range global weather forecasting with 3D neural networks. *Nature*, 619(7970), 533–538. <https://doi.org/10.1038/s41586-023-06185-3>

Bonev, B., Kurth, T., Hundt, C., Pathak, J., Baust, M., Kashinath, K., & Anandkumar, A. (2023). Spherical Fourier Neural Operators: Learning Stable Dynamics on the Sphere (Version 1). <https://doi.org/10.48550/ARXIV.2306.03838>

Brunet, G., Shapiro, M., Hoskins, B., Moncrieff, M., Dole, R., Kiladis, G. N., et al. (2010). Collaboration of the Weather and Climate Communities to Advance Subseasonal-to-Seasonal Prediction. *Bulletin of the American Meteorological Society*, 91(10), 1397–1406. <https://doi.org/10.1175/2010BAMS3013.1>

Bushuk, M., Zhang, Y., Winton, M., Hurlin, B., Delworth, T., Lu, F., et al. (2022). Mechanisms of Regional Arctic Sea Ice Predictability in Two Dynamical Seasonal Forecast Systems. *Journal of Climate*, 35(13), 4207–4231. <https://doi.org/10.1175/JCLI-D-21-0544.1>

Charney, J. G. (1963). A Note on Large-Scale Motions in the Tropics. *Journal of the Atmospheric Sciences*, 20(6), 607–609. [https://doi.org/10.1175/1520-0469\(1963\)020<0607:ANOLSM>2.0.CO;2](https://doi.org/10.1175/1520-0469(1963)020<0607:ANOLSM>2.0.CO;2)

Chen, J.-H., & Lin, S.-J. (2013). Seasonal Predictions of Tropical Cyclones Using a 25-km-Resolution General Circulation Model. *Journal of Climate*, 26(2), 380–398. <https://doi.org/10.1175/JCLI-D-12-00061.1>

Cresswell-Clay, N., Liu, B., Durran, D., Liu, A., Espinosa, Z. I., Moreno, R., & Karlbauer, M. (2024). A Deep Learning Earth System Model for Stable and Efficient Simulation of the Current Climate (Version 1). arXiv. <https://doi.org/10.48550/ARXIV.2409.16247>

Delworth, T. L., Cooke, W. F., Adcroft, A., Bushuk, M., Chen, J., Dunne, K. A., et al. (2020).

SPEAR: The Next Generation GFDL Modeling System for Seasonal to Multidecadal Prediction and Projection. *Journal of Advances in Modeling Earth Systems*, 12(3).

<https://doi.org/10.1029/2019MS001895>

Dulac, W., Cattiaux, J., Chauvin, F., Bourdin, S., & Fromang, S. (2024). Assessing the representation of tropical cyclones in ERA5 with the CNRM tracker. *Climate Dynamics*, 62(1), 223–238. <https://doi.org/10.1007/s00382-023-06902-8>

Emanuel, K., Fondriest, F., & Kossin, J. (2012). Potential Economic Value of Seasonal Hurricane Forecasts. *Weather, Climate, and Society*, 4(2), 110–117.

<https://doi.org/10.1175/WCAS-D-11-00017.1>

Gray, W. M. (1984). Atlantic Seasonal Hurricane Frequency. Part I: El Niño and 30 mb Quasi-Biennial Oscillation Influences. *Monthly Weather Review*, 112(9), 1649–1668.

[https://doi.org/10.1175/1520-0493\(1984\)112<1649:ASHFPI>2.0.CO;2](https://doi.org/10.1175/1520-0493(1984)112<1649:ASHFPI>2.0.CO;2)

Hersbach, H., Bell, B., Berrisford, P., Hirahara, S., Horányi, A., Muñoz-Sabater, J., et al. (2020). The ERA5 global reanalysis. *Quarterly Journal of the Royal Meteorological Society*, 146(730), 1999–2049. <https://doi.org/10.1002/qj.3803>

Hoskins, B. (2013). The potential for skill across the range of the seamless weather-climate prediction problem: a stimulus for our science. *Quarterly Journal of the Royal Meteorological Society*, 139(672), 573–584. <https://doi.org/10.1002/qj.1991>

Keisler, R. (2022). Forecasting Global Weather with Graph Neural Networks (Version 1). <https://doi.org/10.48550/ARXIV.2202.07575>

Knapp, K. R., Kruk, M. C., Levinson, D. H., Diamond, H. J., & Neumann, C. J. (2010). The International Best Track Archive for Climate Stewardship (IBTrACS): Unifying Tropical

Cyclone Data. *Bulletin of the American Meteorological Society*, 91(3), 363–376.

<https://doi.org/10.1175/2009BAMS2755.1>

Kochkov, D., Yuval, J., Langmore, I., Norgaard, P., Smith, J., Mooers, G., et al. (2024). Neural general circulation models for weather and climate. *Nature*.

<https://doi.org/10.1038/s41586-024-07744-y>

Johnson, S. J., Stockdale, T. N., Ferranti, L., Balmaseda, M. A., Molteni, F., Magnusson, L., et al. (2019). SEAS5: The new ECMWF seasonal forecast system. *Geoscientific Model Development*, 12(3), 1087–1117. <https://doi.org/10.5194/gmd-12-1087-2019>

Lam, R., Sanchez-Gonzalez, A., Willson, M., Wirnsberger, P., Fortunato, M., Alet, F., et al. (2023). Learning skillful medium-range global weather forecasting. *Science*, 382(6677), 1416–1421. <https://doi.org/10.1126/science.adf2336>

Lang, S., Alexe, M., Chantry, M., Dramsch, J., Pinault, F., Raoult, B., et al. (2024). AIFS -- ECMWF's data-driven forecasting system (Version 2). arXiv.

<https://doi.org/10.48550/ARXIV.2406.01465>

Lemoine, D., & Kapnick, S. (2024). Financial markets value skillful forecasts of seasonal climate. *Nature Communications*, 15(1), 4059. <https://doi.org/10.1038/s41467-024-48420-z>

Manabe, S., Holloway, J. L., & Stone, H. M. (1970). Tropical Circulation in a Time-Integration of a Global Model of the Atmosphere. *Journal of the Atmospheric Sciences*, 27(4), 580–613. [https://doi.org/10.1175/1520-0469\(1970\)027<0580:TCIATI>2.0.CO;2](https://doi.org/10.1175/1520-0469(1970)027<0580:TCIATI>2.0.CO;2)

Pathak, J., Subramanian, S., Harrington, P., Raja, S., Chattopadhyay, A., Mardani, M., et al. (2022). FourCastNet: A Global Data-driven High-resolution Weather Model using

Adaptive Fourier Neural Operators (Version 1).

<https://doi.org/10.48550/ARXIV.2202.11214>

Phillips, N. A. (1956). The general circulation of the atmosphere: A numerical experiment.

*Quarterly Journal of the Royal Meteorological Society*, 82(352), 123–164.

<https://doi.org/10.1002/qj.49708235202>

Price, I., Sanchez-Gonzalez, A., Alet, F., Ewalds, T., El-Kadi, A., Stott, J., et al. (2023).

GenCast: Diffusion-based ensemble forecasting for medium-range weather (Version 1).

<https://doi.org/10.48550/ARXIV.2312.15796>

Roberts, M. J., Camp, J., Seddon, J., Vidale, P. L., Hodges, K., Vanniere, B., et al. (2020).

Impact of Model Resolution on Tropical Cyclone Simulation Using the HighResMIP–PRIMAVERA Multimodel Ensemble. *Journal of Climate*, 33(7), 2557–2583.

<https://doi.org/10.1175/JCLI-D-19-0639.1>

Roberts, M. J., Camp, J., Seddon, J., Vidale, P. L., Hodges, K., Vannière, B., et al. (2020).

Projected Future Changes in Tropical Cyclones Using the CMIP6 HighResMIP Multimodel Ensemble. *Geophysical Research Letters*, 47(14).

<https://doi.org/10.1029/2020GL088662>

Shukla, J. (1998). Predictability in the Midst of Chaos: A Scientific Basis for Climate Forecasting. *Science*, 282(5389), 728–731. <https://doi.org/10.1126/science.282.5389.728>

Sobel, A. H., & Bretherton, C. S. (2000). Modeling Tropical Precipitation in a Single Column.

*Journal of Climate*, 13(24), 4378–4392. [https://doi.org/10.1175/1520-0442\(2000\)013<4378:MTPIAS>2.0.CO;2](https://doi.org/10.1175/1520-0442(2000)013<4378:MTPIAS>2.0.CO;2)

Ullrich, P. A., Zarzycki, C. M., McClenny, E. E., Pinheiro, M. C., Stansfield, A. M., & Reed, K. A. (2021). TempestExtremes v2.1: a community framework for feature detection,

tracking, and analysis in large datasets. *Geoscientific Model Development*, 14(8), 5023–5048. <https://doi.org/10.5194/gmd-14-5023-2021>

Vecchi, G. A., Delworth, T., Gudgel, R., Kapnick, S., Rosati, A., Wittenberg, A. T., et al. (2014). On the Seasonal Forecasting of Regional Tropical Cyclone Activity. *Journal of Climate*, 27(21), 7994–8016. <https://doi.org/10.1175/JCLI-D-14-00158.1>

Vonich, P. T., & Hakim, G. J. (2024). Predictability Limit of the 2021 Pacific Northwest Heatwave From Deep-Learning Sensitivity Analysis. *Geophysical Research Letters*, 51(19), e2024GL110651. <https://doi.org/10.1029/2024GL110651>

Wang, Z., Zhang, G., Dunkerton, T. J., & Jin, F.-F. (2020). Summertime stationary waves integrate tropical and extratropical impacts on tropical cyclone activity. *Proceedings of the National Academy of Sciences*, 117(37), 22720–22726.  
<https://doi.org/10.1073/pnas.2010547117>

Watt-Meyer, O., Henn, B., McGibbon, J., Clark, S. K., Kwa, A., Perkins, W. A., et al. (2024). ACE2: Accurately learning subseasonal to decadal atmospheric variability and forced responses (Version 1). arXiv. <https://doi.org/10.48550/ARXIV.2411.11268>

World Meteorological Organization. (2021). *WMO Atlas of Mortality and Economic Losses from Weather, Climate and Water Extremes (1970–2019) (WMO-No. 1267)*. Geneva: WMO.

Yeager, S. G., Danabasoglu, G., Rosenbloom, N. A., Strand, W., Bates, S. C., Meehl, G. A., et al. (2018). Predicting Near-Term Changes in the Earth System: A Large Ensemble of Initialized Decadal Prediction Simulations Using the Community Earth System Model. *Bulletin of the American Meteorological Society*, 99(9), 1867–1886.  
<https://doi.org/10.1175/BAMS-D-17-0098.1>

Yuval, J., Langmore, I., Kochkov, D., & Hoyer, S. (2024). Neural general circulation models optimized to predict satellite-based precipitation observations (Version 1). arXiv. <https://doi.org/10.48550/ARXIV.2412.11973>

Zhang, G., Wang, Z., Dunkerton, T. J., Peng, M. S., & Magnusdottir, G. (2016). Extratropical Impacts on Atlantic Tropical Cyclone Activity. *Journal of the Atmospheric Sciences*, 73(3), 1401–1418. <https://doi.org/10.1175/JAS-D-15-0154.1>

Zhang, G., Murakami, H., Gudgel, R., & Yang, X. (2019). Dynamical Seasonal Prediction of Tropical Cyclone Activity: Robust Assessment of Prediction Skill and Predictability. *Geophysical Research Letters*, 46(10), 5506–5515.

<https://doi.org/10.1029/2019GL082529>

Zhang, G., Murakami, H., Yang, X., Findell, K. L., Wittenberg, A. T., & Jia, L. (2021). Dynamical Seasonal Predictions of Tropical Cyclone Activity: Roles of Sea Surface Temperature Errors and Atmosphere–Land Initialization. *Journal of Climate*, 34(5), 1743–1766. <https://doi.org/10.1175/JCLI-D-20-0215.1>

Zhao, M., Held, I. M., Lin, S.-J., & Vecchi, G. A. (2009). Simulations of Global Hurricane Climatology, Interannual Variability, and Response to Global Warming Using a 50-km Resolution GCM. *Journal of Climate*, 22(24), 6653–6678.

<https://doi.org/10.1175/2009JCLI3049.1>

Zhao, M., Held, I. M., & Vecchi, G. A. (2010). Retrospective Forecasts of the Hurricane Season Using a Global Atmospheric Model Assuming Persistence of SST Anomalies. *Monthly Weather Review*, 138(10), 3858–3868. <https://doi.org/10.1175/2010MWR3366.1>

Supplementary Materials for

**Seasonal Prediction with Neural GCM and Simplified Boundary Forcings:  
Large-scale Atmospheric Variability and Tropical Cyclone Activity**

Gan Zhang<sup>1\*</sup>, Megha Rao<sup>1</sup>, Janni Yuval<sup>2</sup>, Ming Zhao<sup>3</sup>

<sup>1</sup> Department of Climate, Meteorology, and Atmospheric Sciences, University of Illinois at Urbana-Champaign

<sup>2</sup> Google Research

<sup>3</sup> Geophysical Fluid Dynamics Laboratory, National Oceanic and Atmospheric Administration

File Content

Supplementary Text

Supplementary Figures 1–20

Supplementary Table 1

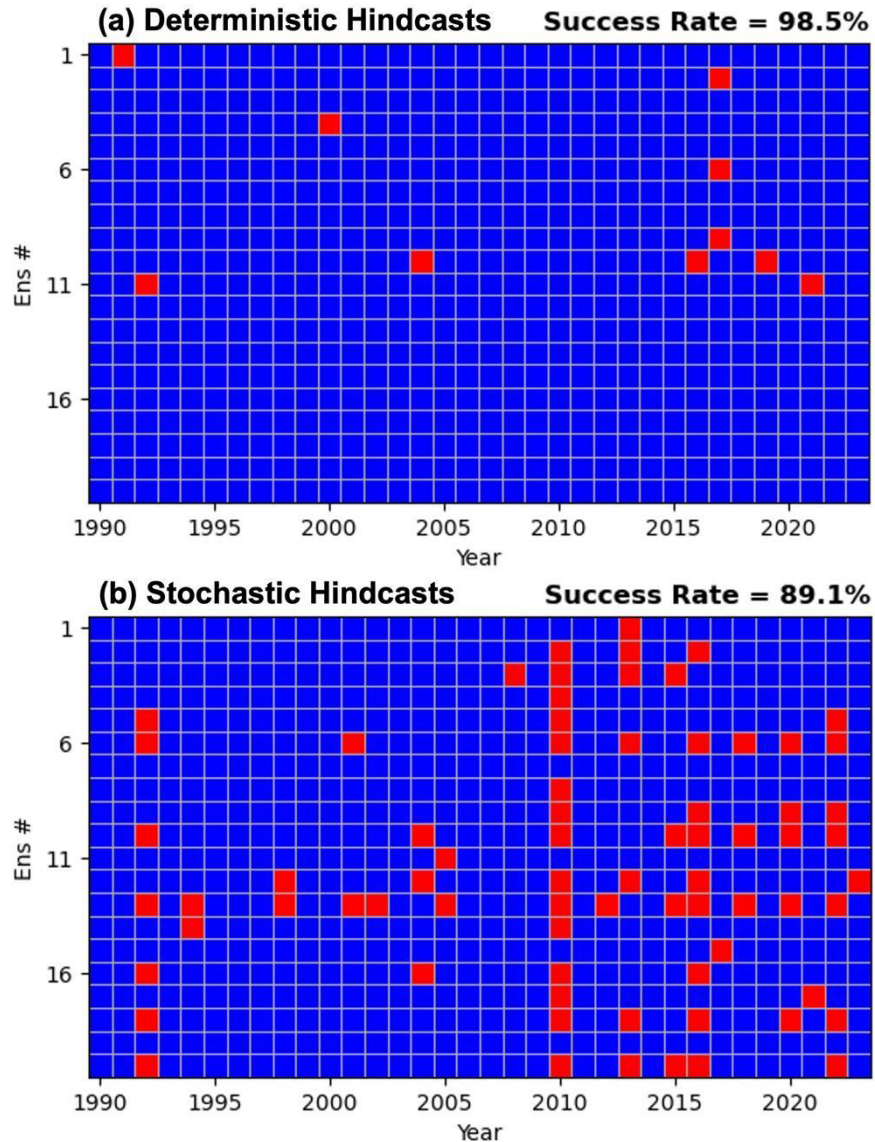
## Considerations for Model Evaluation

This study produces and evaluates the NeuralGCM's performance with simplified boundary conditions for seasonal prediction tasks. While this provides a valuable baseline, it represents a lower-bound estimate of the model's potential skill due to several limitations, primarily stemming from the simplified boundary forcing used to generate the hindcast and the biases of inherited from the training dataset (i.e., ERA5) in representing tropical cyclones. Direct comparisons with operational seasonal prediction models are challenging due to data accessibility. While some model output is publicly available, the specific variables and temporal resolution required for a fair comparison are often not readily accessible. For instance, 6-hourly surface pressure and upper-air fields, crucial for detailed verification and tropical cyclone tracking, are not consistently archived or distributed by public service. Furthermore, the NeuralGCM version used by this study does not directly output precipitation or surface temperature, two key variables for many forecast applications. Additionally, the boundary forcings and the representation of coupled processes differ substantially between this NeuralGCM configuration and the operational prediction systems. This issue makes it hard to attribute the sources of skill differences, limiting scientific insights that can be yielded by direct comparisons. To facilitate preliminary comparisons of prediction skill, we include anomaly correlation coefficients of an operational seasonal prediction system (Johnson et al. 2019) and the observation for a set of available variables (Supplementary Figures 12-14). A more comprehensive evaluation needs to involve collaboration with developers of operational seasonal prediction models to establish a standardized comparison framework, including common output variables and metrics, facilitating a more rigorous and insightful assessment of the model capabilities.

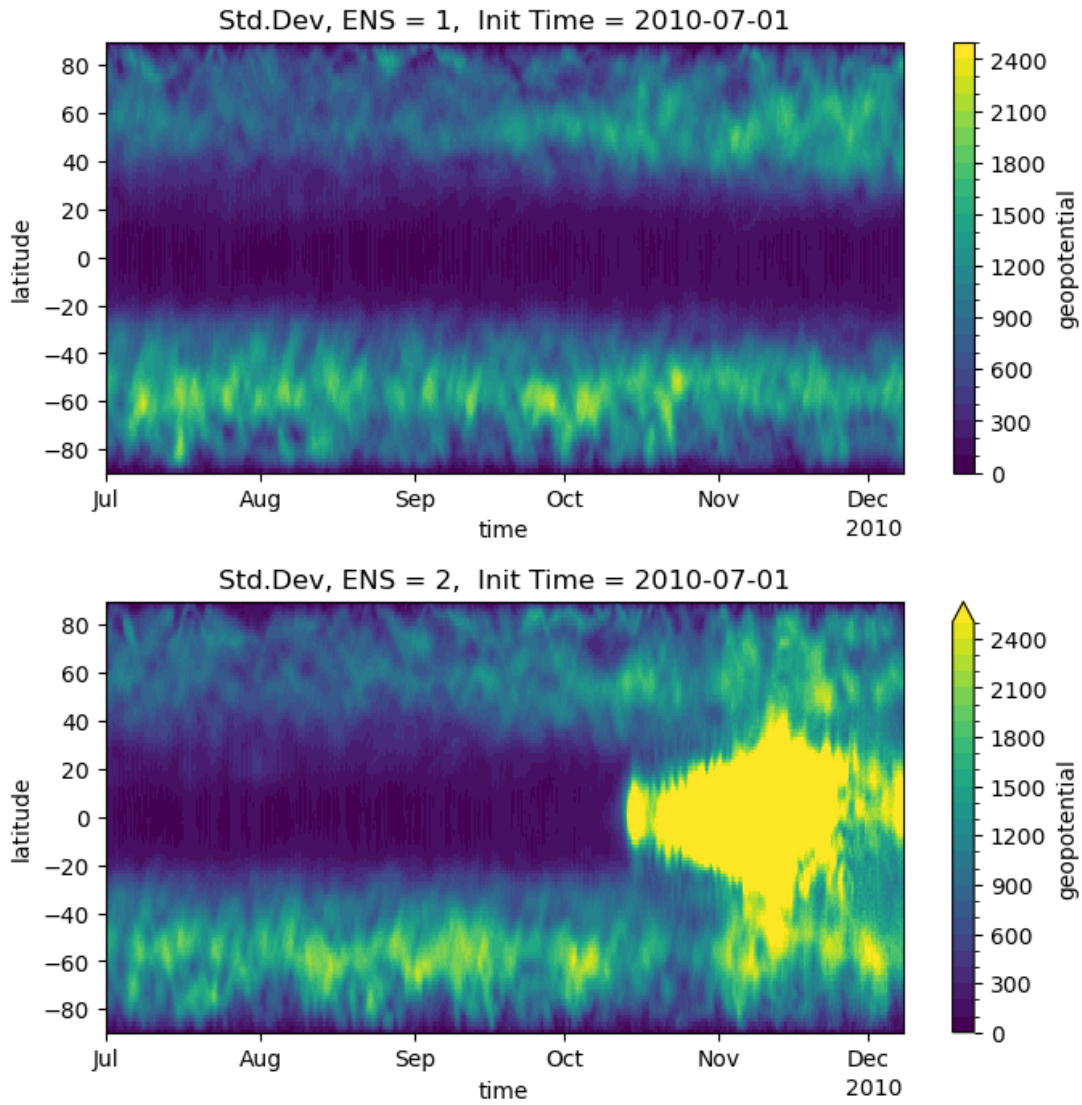
## Comparisons of NeuralGCM Hindcasts with Deterministic and Stochastic Physics

These hindcasts show similar skills in predicting TC metrics, but their simulation stability and biases appear to have notable differences. For instance, the hindcast simulations with stochastic physics have a higher chance to encounter issues with spurious waves in the tropics (main text and Supplementary Figures 1-2). The hindcast simulations with deterministic physics appear more likely to generate large biases in polar regions, which contribute to large errors in Supplementary Figures 5 and 9. Such large polar biases are not apparent in the hindcast simulations with stochastic

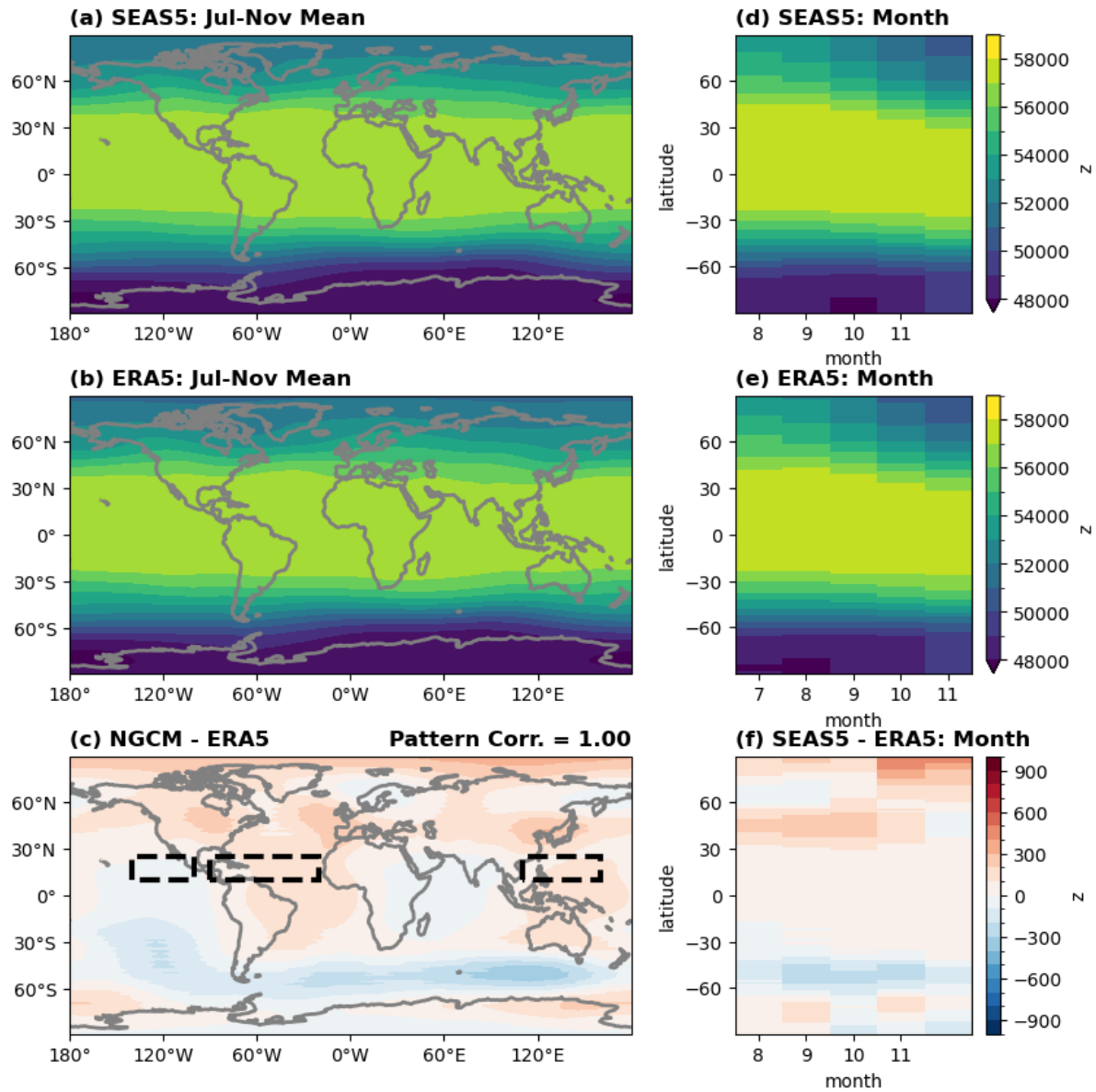
physics. More detailed comparisons between the models with deterministic and stochastic physics will be conducted after an update of the NeuralGCM.



Supplementary Figure 1 *An overview of rollout instability in the NeuralGCM hindcasts. (a) Hindcasts with the deterministic physics. (b) Hindcasts with the stochastic model physics. The instability cases are flagged with red coloring. The percentage of simulations that passed the stability test is denoted in the top right of subplots.*

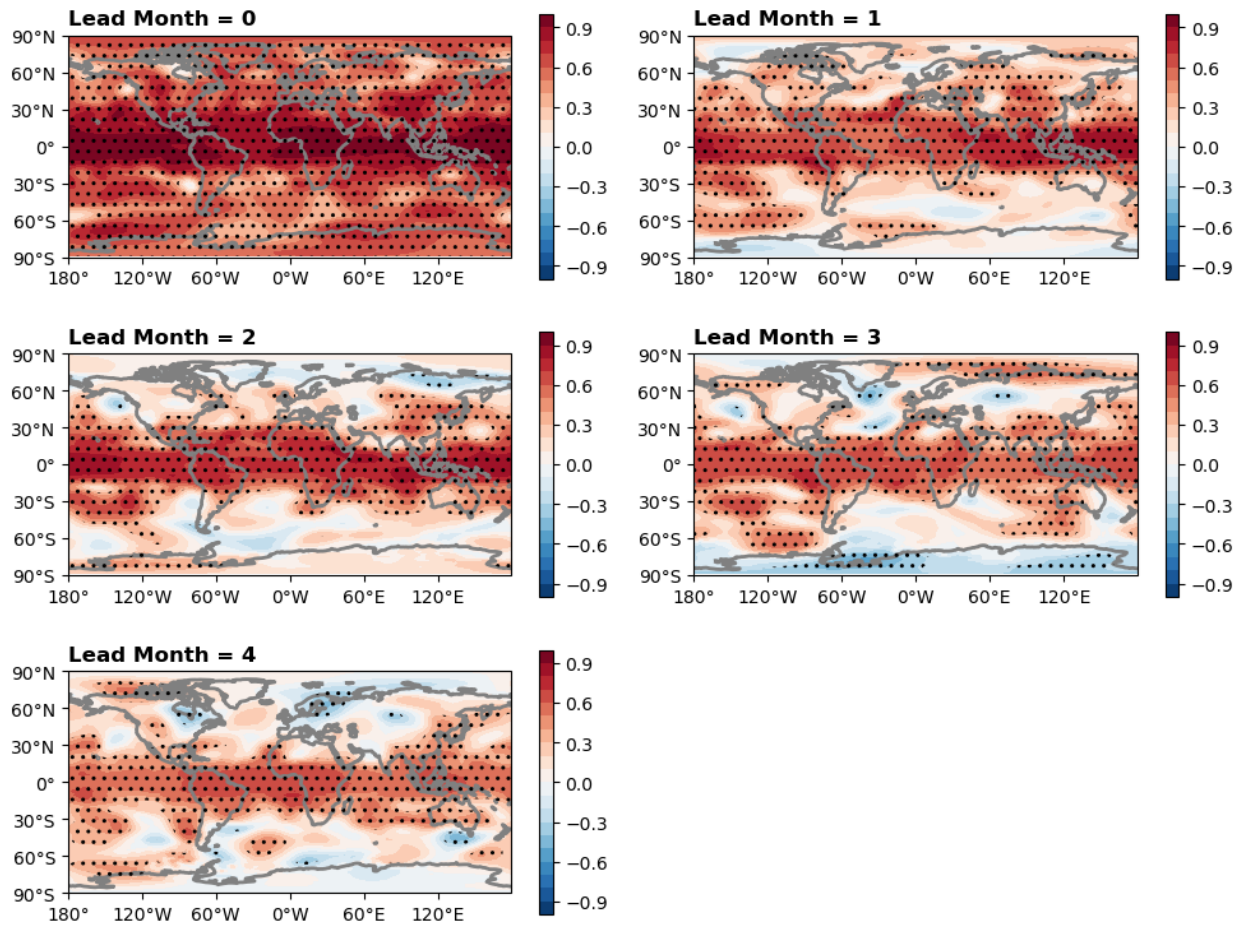


Supplementary Figure 2 *Evolution of stable (top) and unstable (bottom) prediction rollouts with stochastic model physics. The field is the standard deviation of the 500-hPa geopotential in the zonal direction. Spurious waves appear in the unstable simulation around mid-October. Both simulations were initialized on July 1, 2010 with slightly different random seeding.*



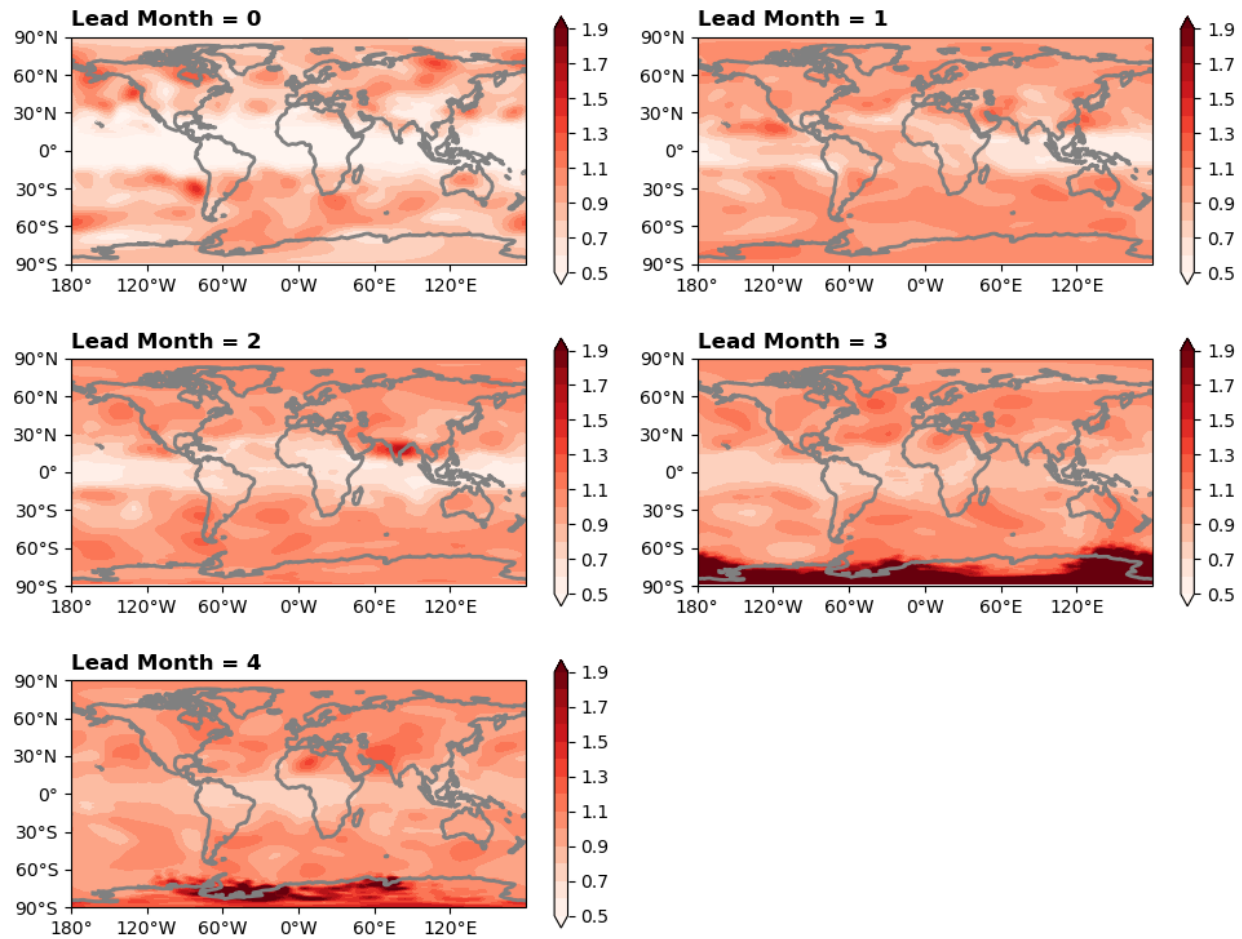
Supplementary Figure 3 *The climatology of 500-hPa geopotential height of the ECMWF's fifth generation seasonal forecast system (SEAS5). The data of SEAS5 (version 5.1) of 1990-2019 are regridded to the NeuralGCM grid. The original SEAS5 data has 25 ensemble members for simulations initialized in 1990-2016 and 51 for simulations initialized in 2017-2019. The analyses only consider the first 20 ensemble members to ensure the ensemble size is consistent with the NeuralGCM hindcasts. The plotting settings are the same as Figure 1.*

**500 hPa Geopotential Anom Corr.**  
**Initialization: 07-01 (1990-2023)**



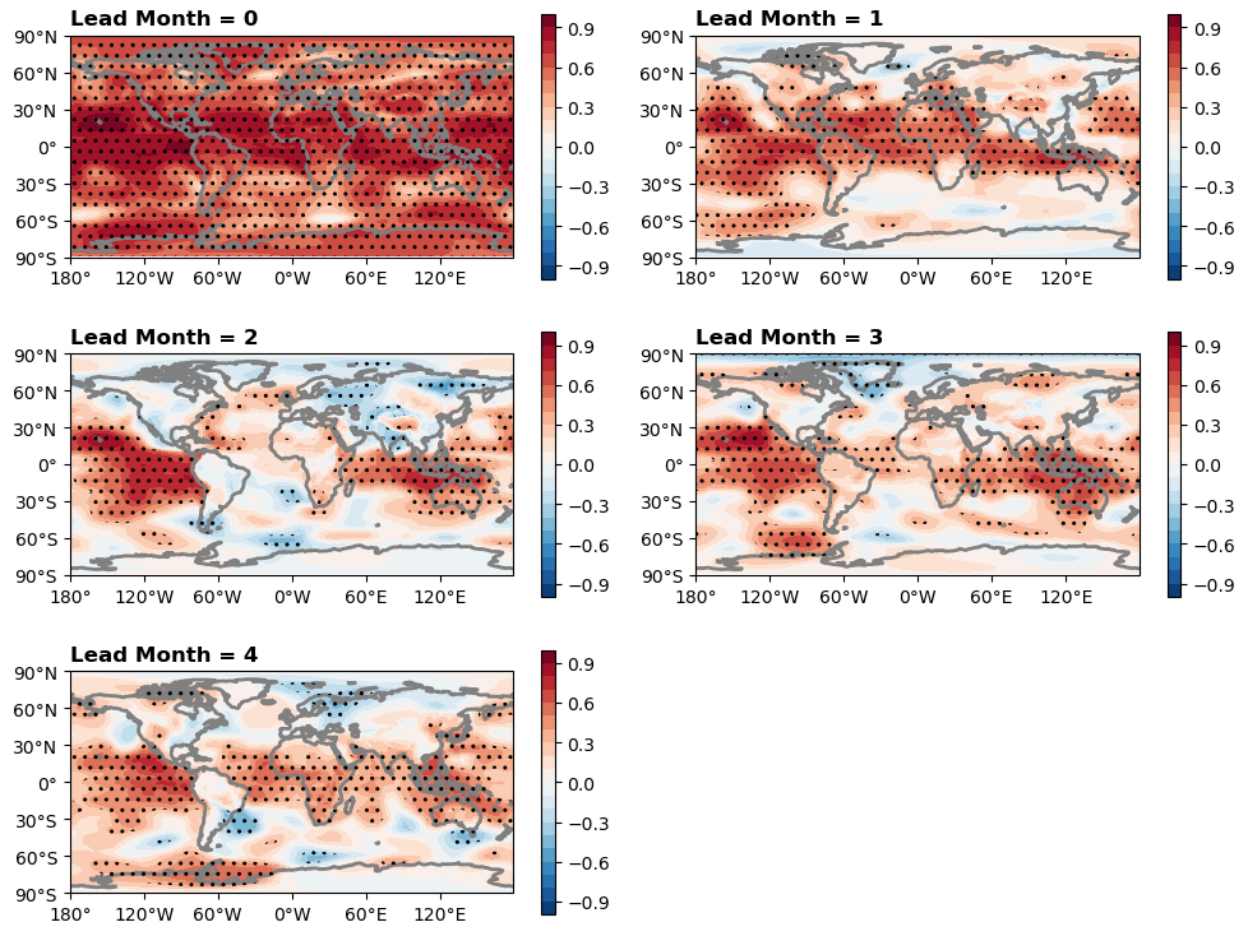
Supplementary Figure 4 *Anomaly correlation coefficients of the 500-hPa geopotential height between the NeuralGCM hindcasts and the ERA5 reference. (a) Lead Month 0 (July), (b) Lead Month 1 (August), (c) Lead Month 2 (September), (d) Lead Month 3 (October), (e) Lead Month 4 (November). The stippling indicates parts above the 90% confidence level.*

**500 hPa Geopotential Normalized RMSE**  
**Initialization: 07-01 (1990-2023)**



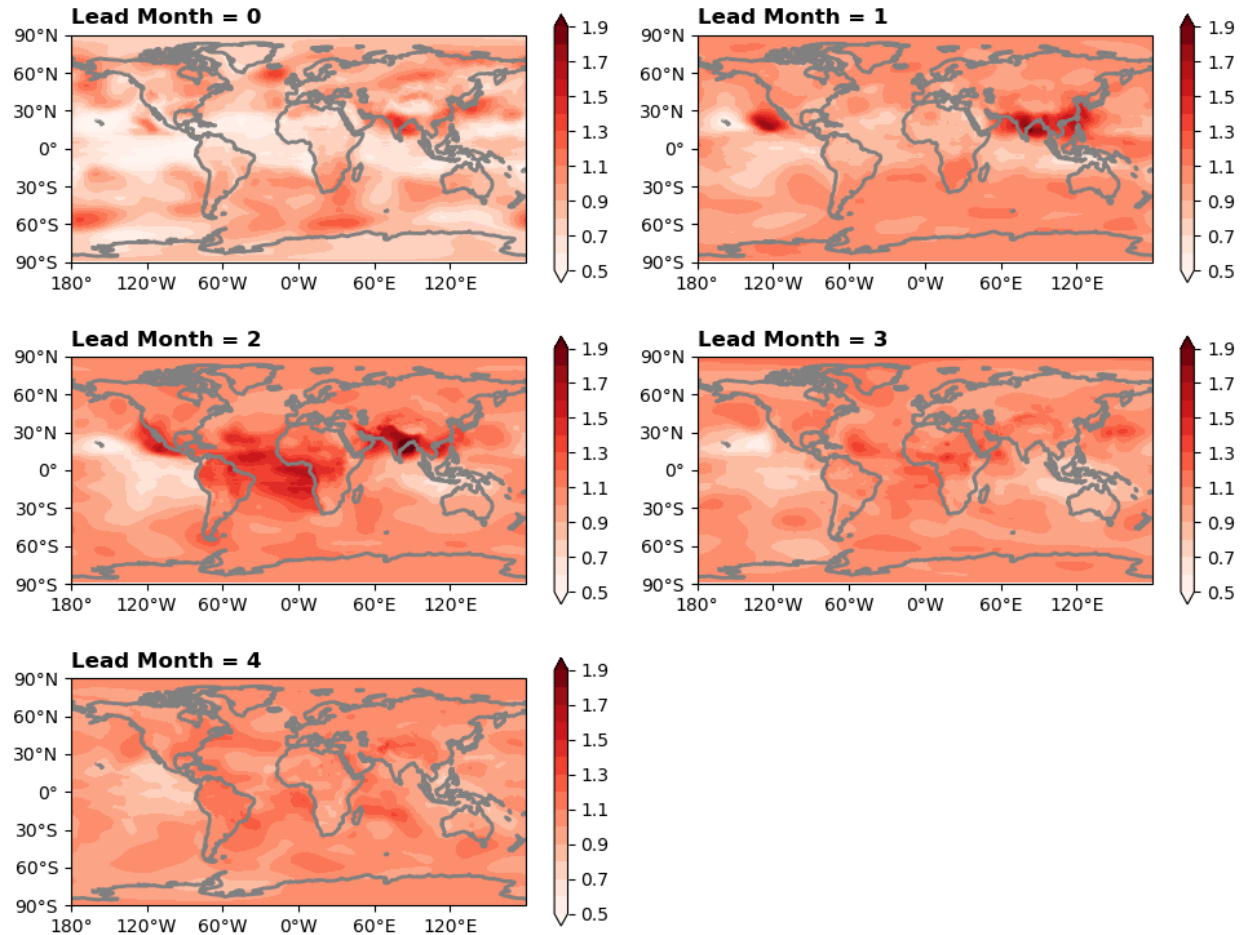
Supplementary Figure 5 *Normalized root mean squared error (RMSE) of the 500-hPa geopotential height between the NeuralGCM hindcasts and the ERA5 reference. (a) Lead Month 0 (July), (b) Lead Month 1 (August), (c) Lead Month 2 (September), (d) Lead Month 3 (October), (e) Lead Month 4 (November). The RMSE is normalized with the standard deviation of the ERA5 reference.*

**Surface Pressure Anomalous Corr.**  
**Initialization: 07-01 (1990-2023)**



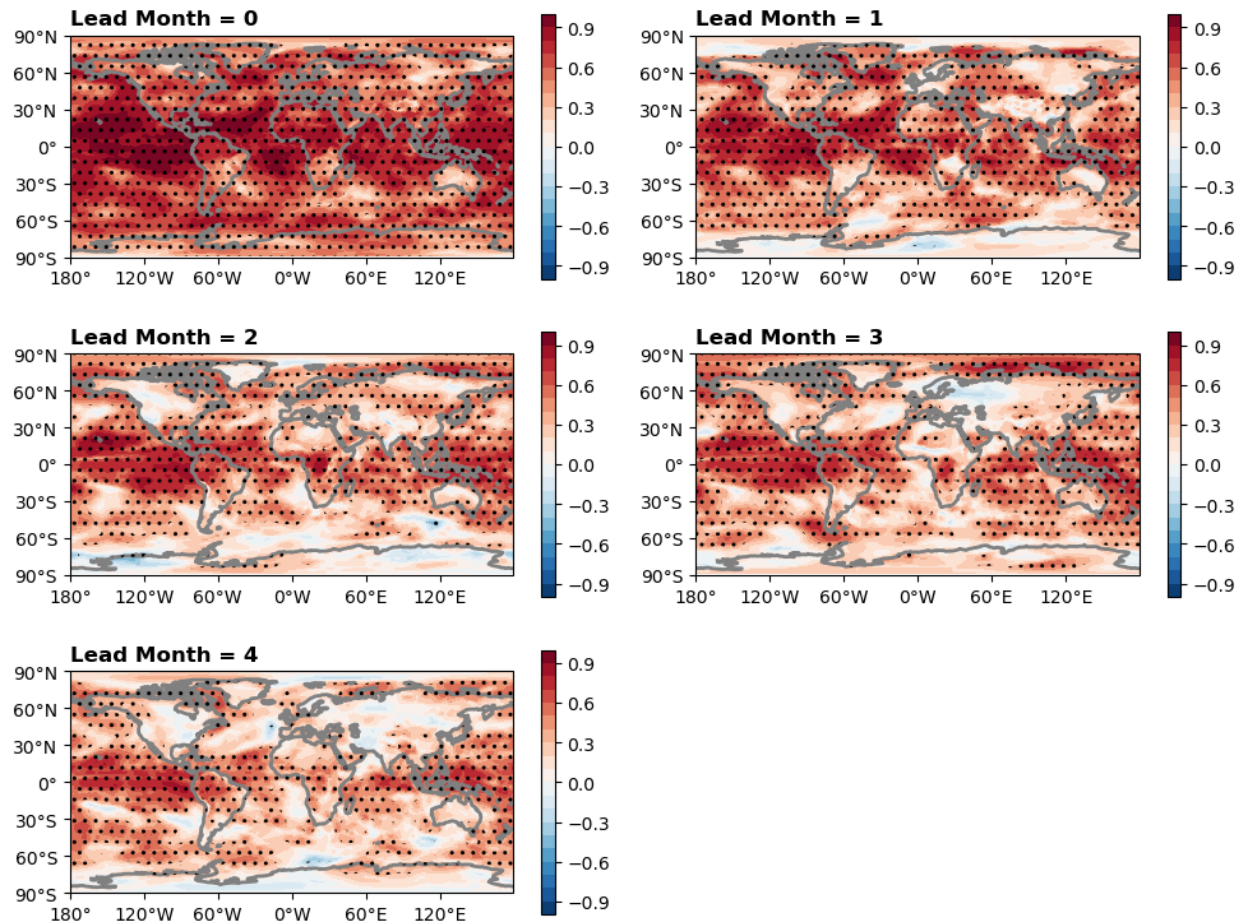
Supplementary Figure 6 *Anomaly correlation coefficients of the surface pressure between the NeuralGCM hindcasts and the ERA5 reference. The other settings are the same as in Supplementary Figure 4.*

**Surface Pressure Normalized RMSE**  
**Initialization: 07-01 (1990-2023)**



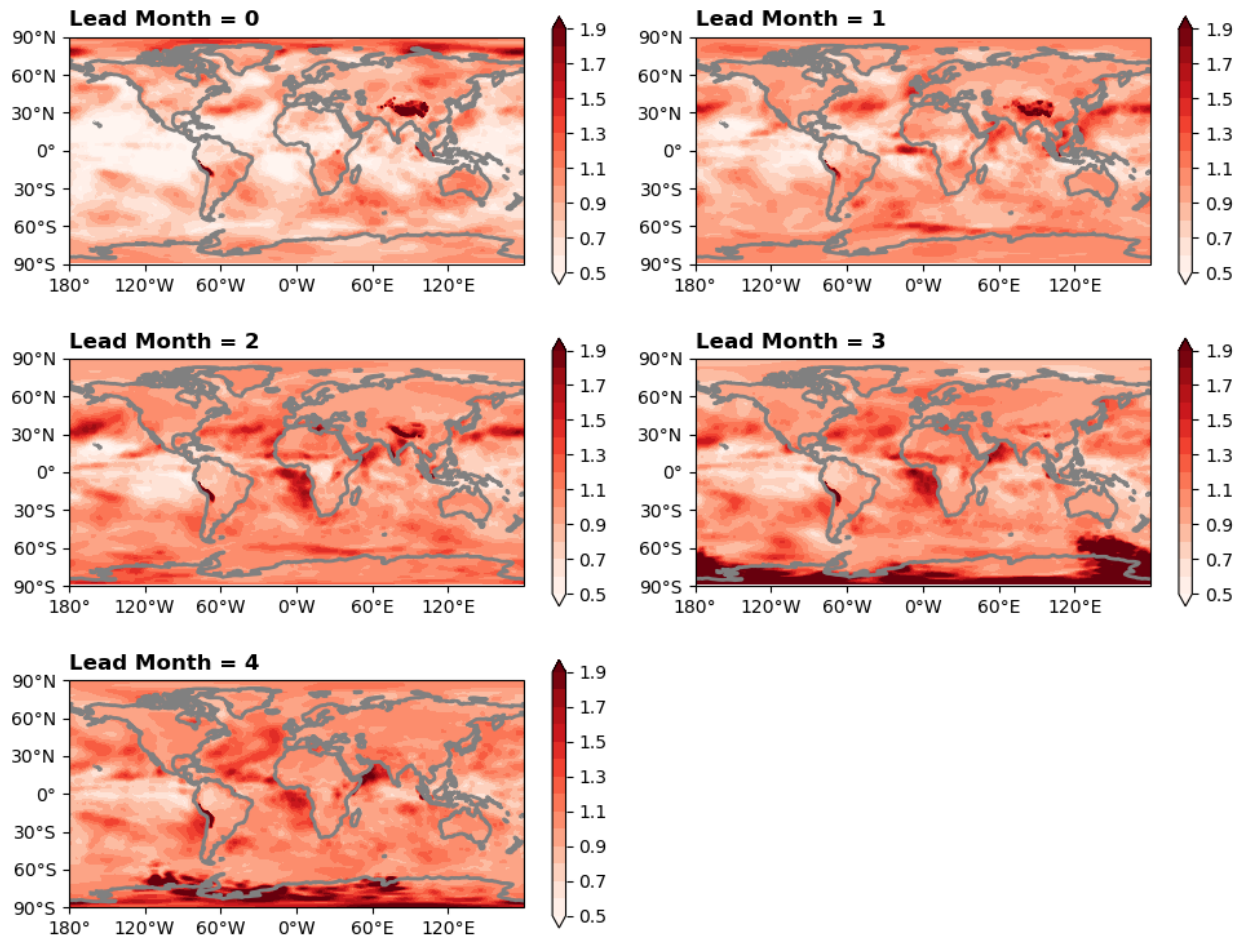
Supplementary Figure 7 *Normalized root mean squared error (RMSE) of the surface pressure between the NeuralGCM hindcasts and the ERA5 reference. The other settings are the same as in Supplementary Figure 5.*

**1000 hPa Temperature Anom Corr.**  
**Initialization: 07-01 (1990-2023)**



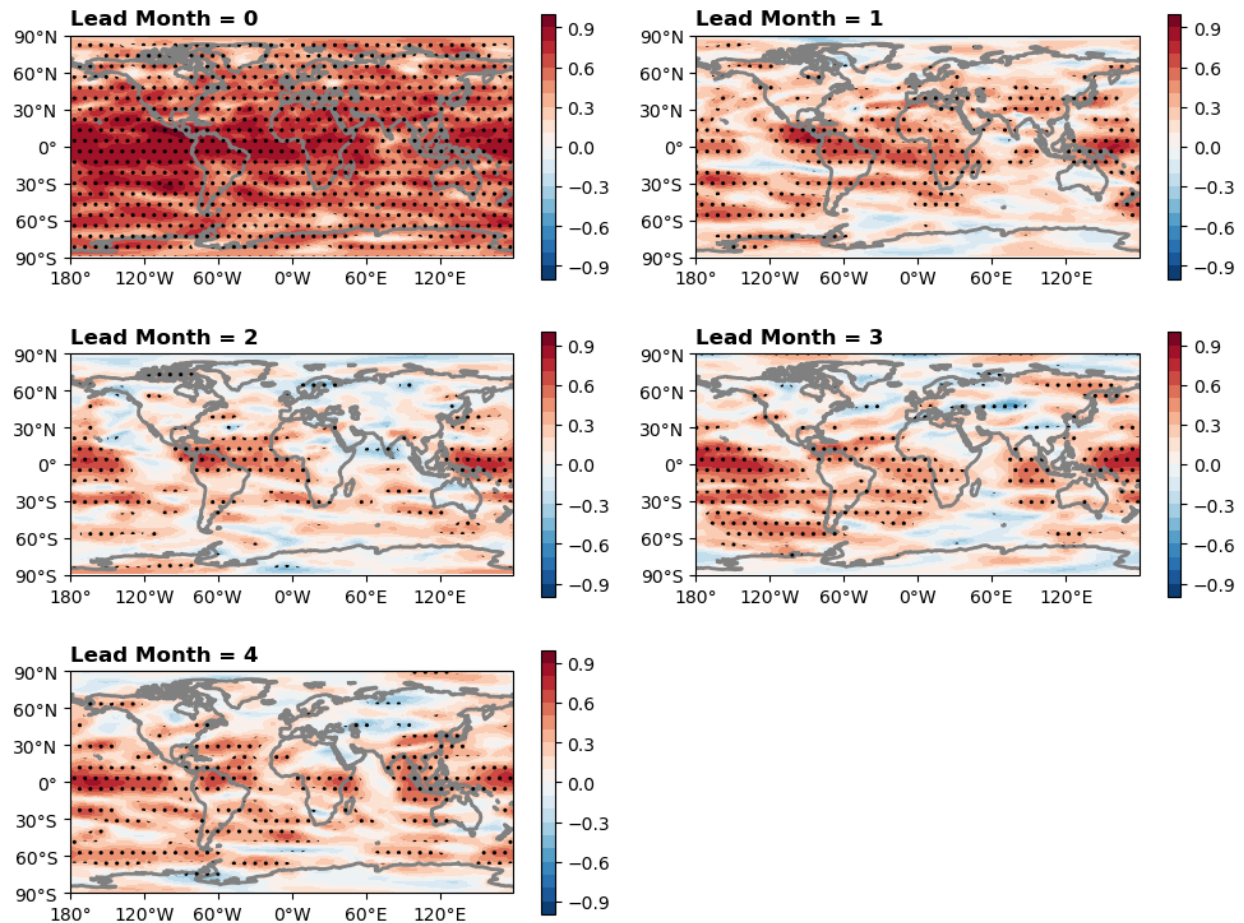
Supplementary Figure 8 *Anomaly correlation coefficients of the 1000-hPa air temperature between the NeuralGCM hindcasts and the ERA5 reference. The other settings are the same as in Supplementary Figure 4.*

**1000 hPa Temperature Normalized RMSE**  
**Initialization: 07-01 (1990-2023)**



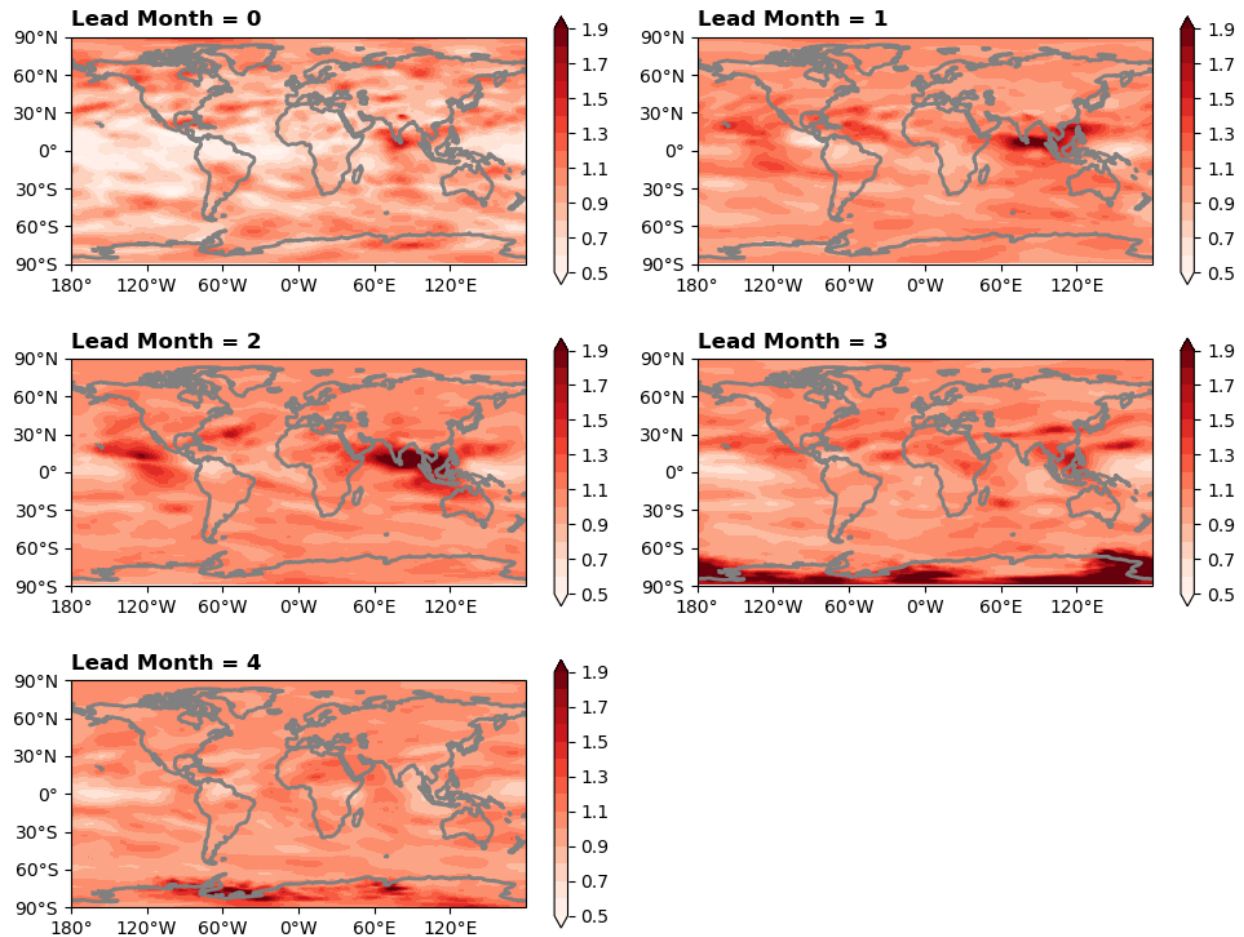
Supplementary Figure 9 *Normalized root mean squared error (RMSE) of the 1000-hPa air temperature between the NeuralGCM hindcasts and the ERA5 reference. The other settings are the same as in Supplementary Figure 5.*

**U Shear Anomalous Corr.**  
**Initialization: 07-01 (1990-2023)**



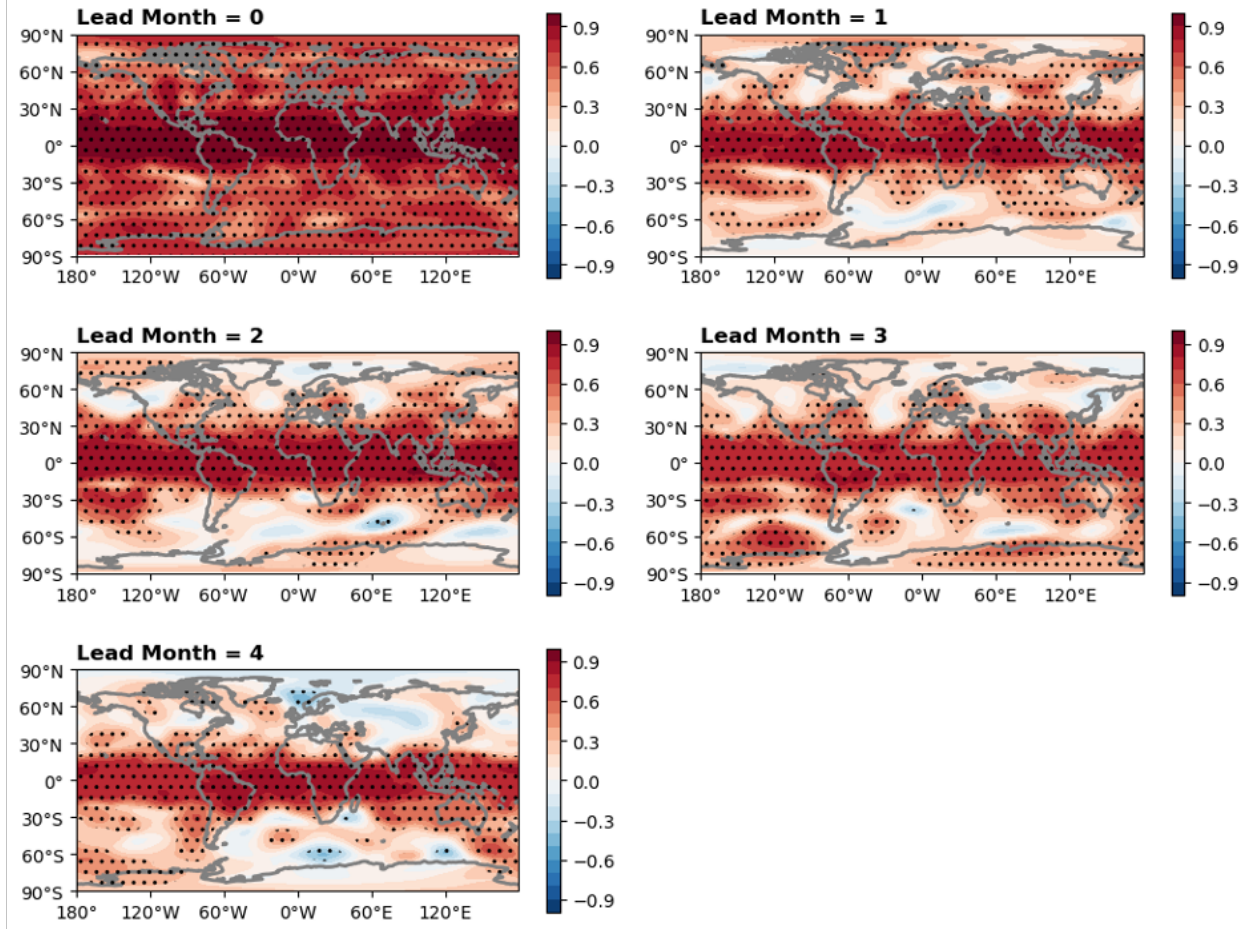
Supplementary Figure 10 *Anomaly correlation coefficients of the zonal wind shear (200 hPa - 850 hPa) between the NeuralGCM hindcasts and the ERA5 reference. The other settings are the same as in Supplementary Figure 4.*

**U Shear Normalized RMSE**  
**Initialization: 07-01 (1990-2023)**



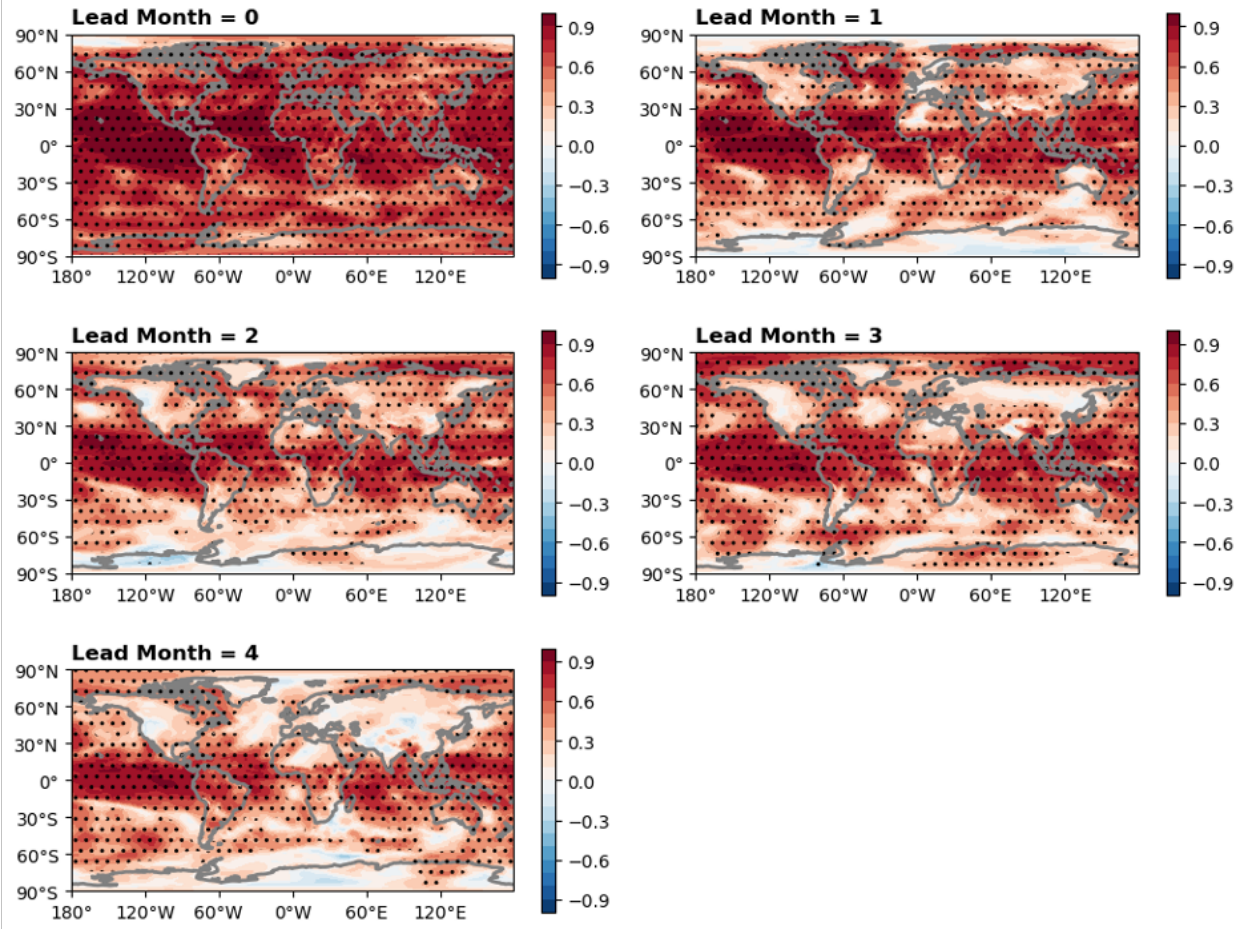
Supplementary Figure 11 *Normalized root mean squared error (RMSE) of the zonal wind shear (200 hPa - 850 hPa) between the NeuralGCM hindcasts and the ERA5 reference. The other settings are the same as in Supplementary Figure 5.*

**SEAS5 500-hPa Geopotential Anomalous Corr.**  
**Initialization: 07-01 (1990-2023)**



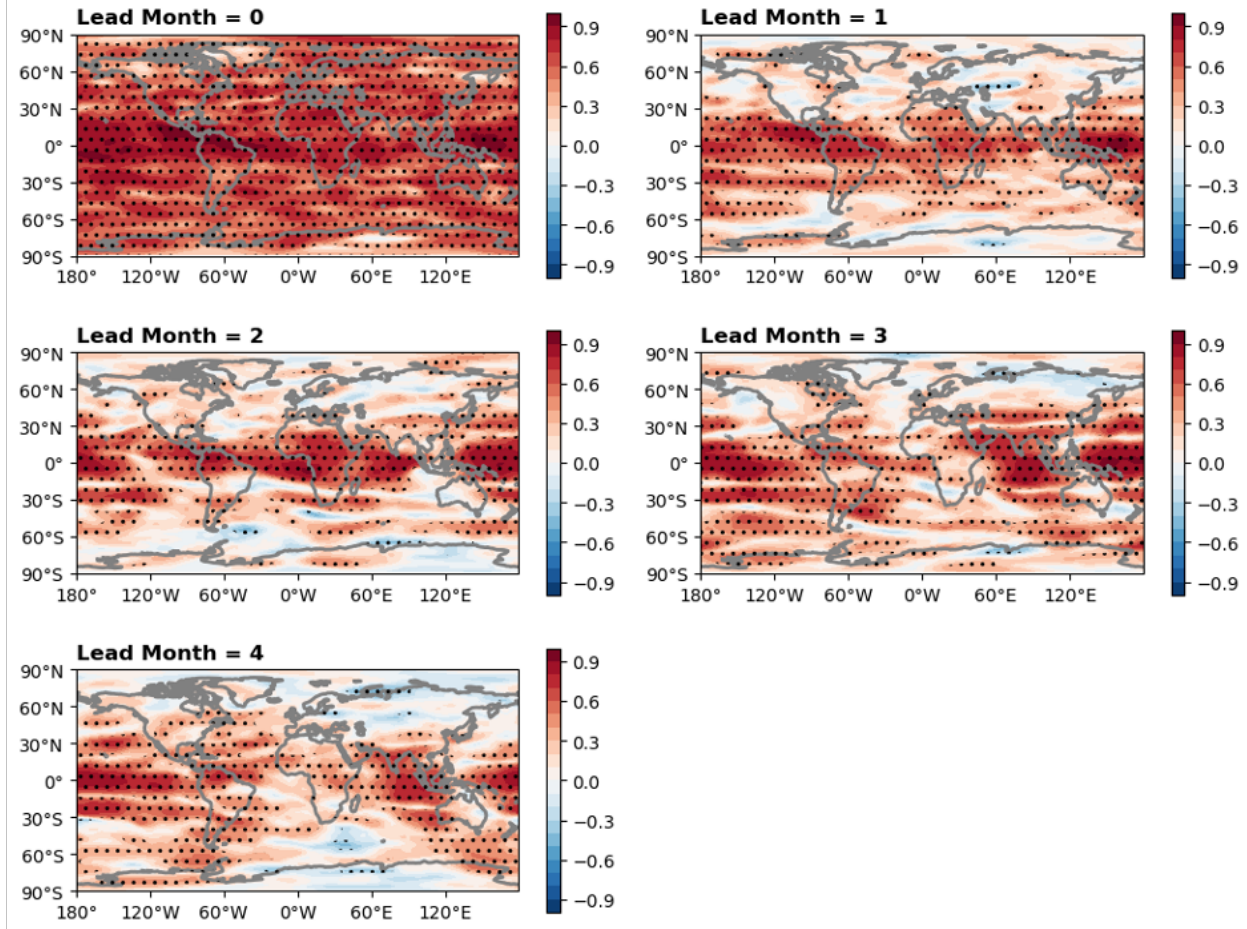
Supplementary Figure 12 *Anomaly correlation coefficients of the 500-hPa geopotential height between the ECWMF SEAS5 and the ERA5 reference. The data of SEAS5 (version 5.1) of 1990-2019 are regressed to the NeuralGCM grid. The analyses only consider the first 20 ensemble members to ensure the ensemble size is consistent with the NeuralGCM hindcasts. The other plotting settings are the same as Supplementary Figure 4.*

**SEAS5 1000-hPa Temperature Anom Corr.**  
**Initialization: 07-01 (1990-2023)**

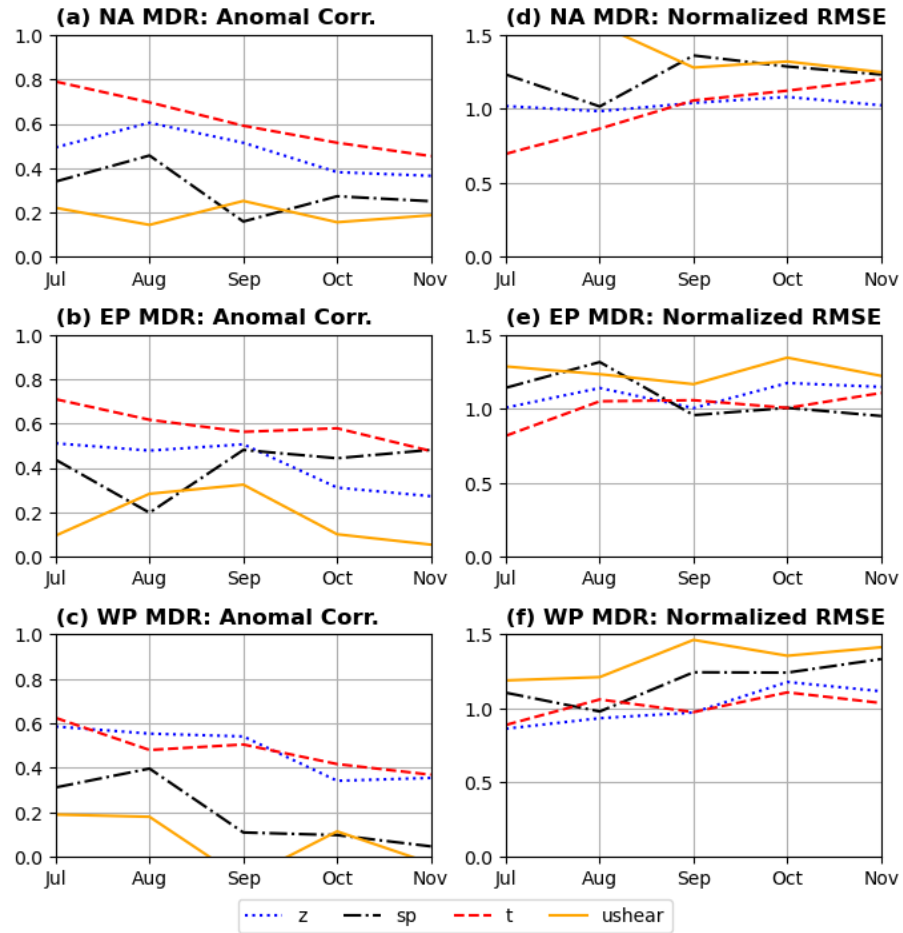


Supplementary Figure 13 *Anomaly correlation coefficients of the 1000-hPa temperature between the ECWMF SEAS5 and the ERA5 reference. The data of SEAS5 (version 5.1) of 1990-2019 are regressed to the NeuralGCM grid. The analyses only consider the first 20 ensemble members to ensure the ensemble size is consistent with the NeuralGCM hindcasts. The other plotting settings are the same as Supplementary Figure 4.*

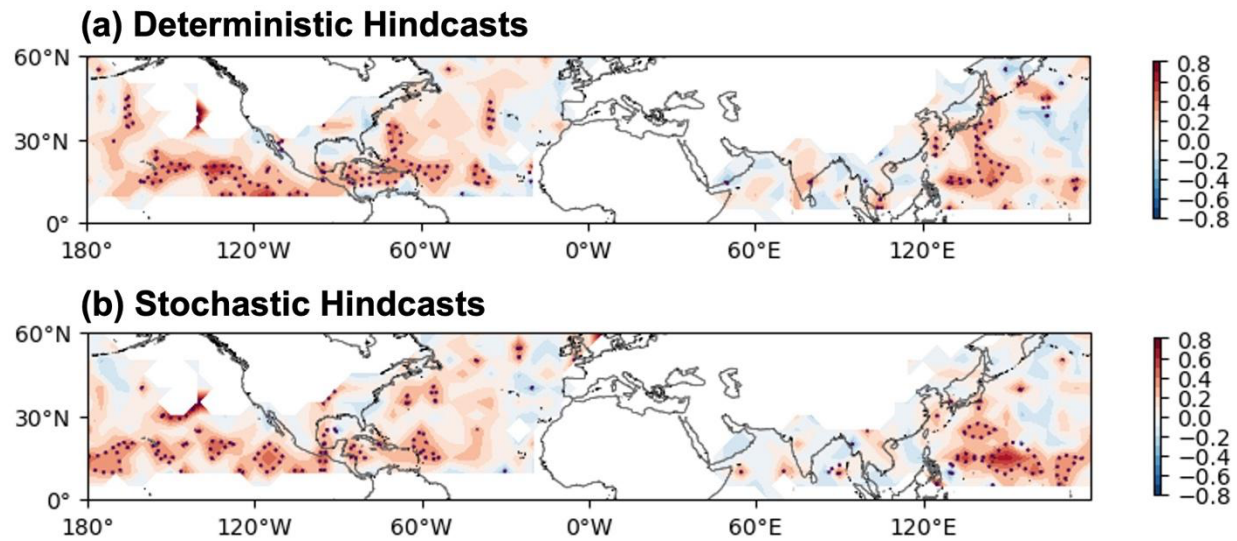
**SEAS5 U Shear Anomalous Corr.**  
**Initialization: 07-01 (1990-2023)**



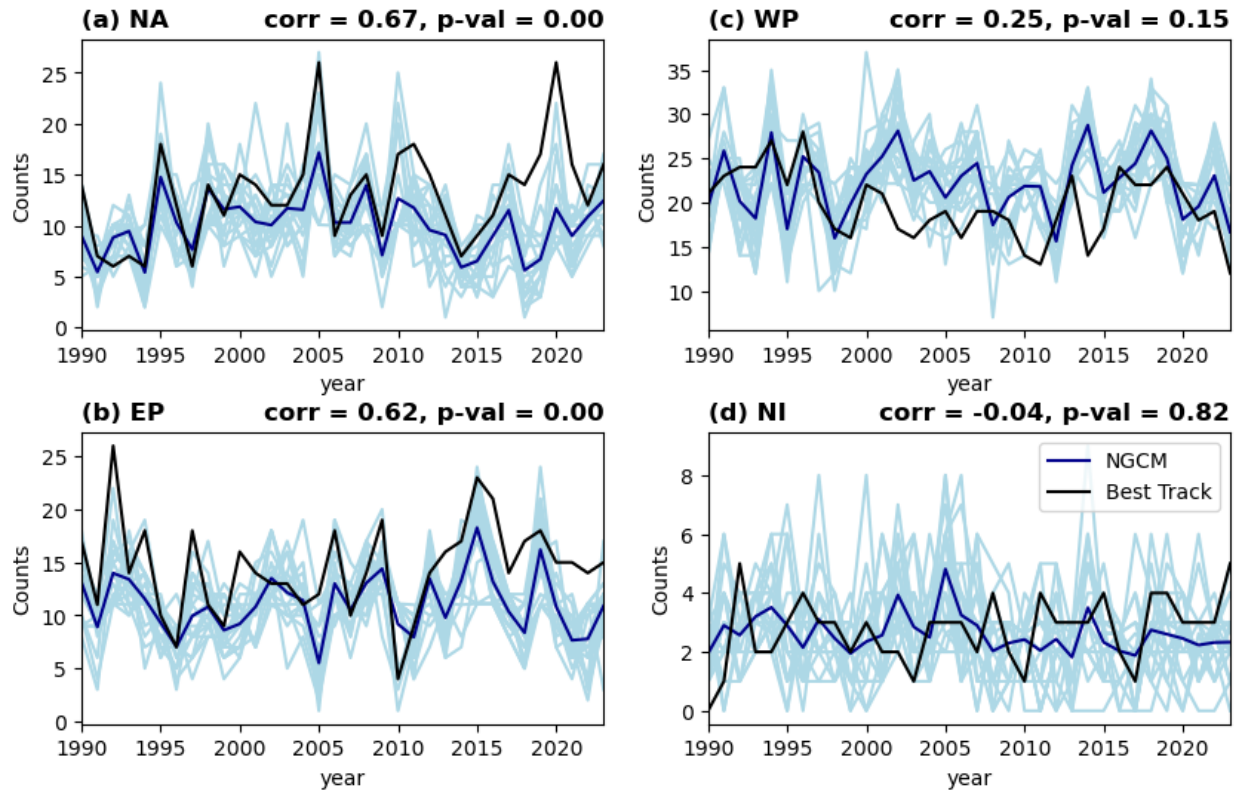
Supplementary Figure 14 *Anomaly correlation coefficients of the 200-hPa and 850-hPa zonal wind shear between the ECWMF SEAS5 and the ERA5 reference. The data of SEAS5 (version 5.1) of 1990-2019 are regressed to the NeuralGCM grid. The analyses only consider the first 20 ensemble members to ensure the ensemble size is consistent with the NeuralGCM hindcasts. All the other settings are the same as Supplementary Figure 4.*



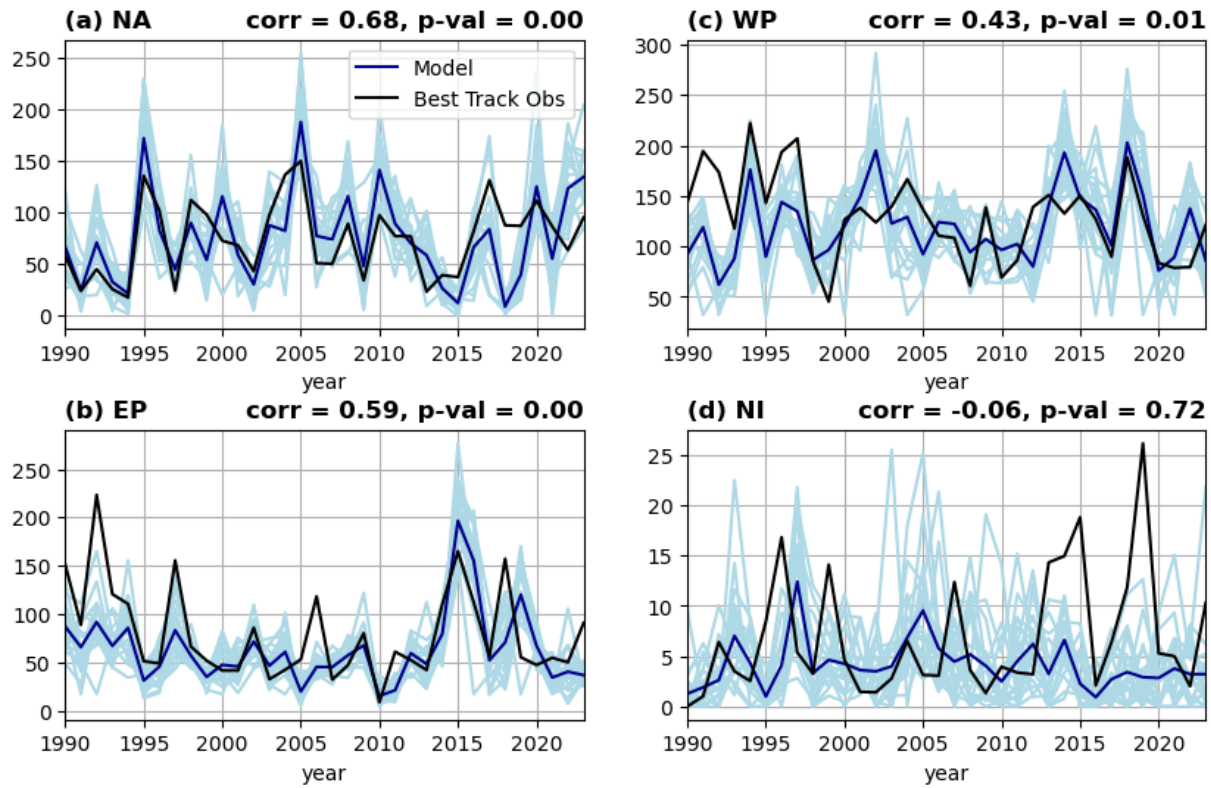
Supplementary Figure 15 *Prediction skills of persisting the monthly mean anomalies of June for the Main Development Regions (MDRs). The other settings are the same as Figure 2.*



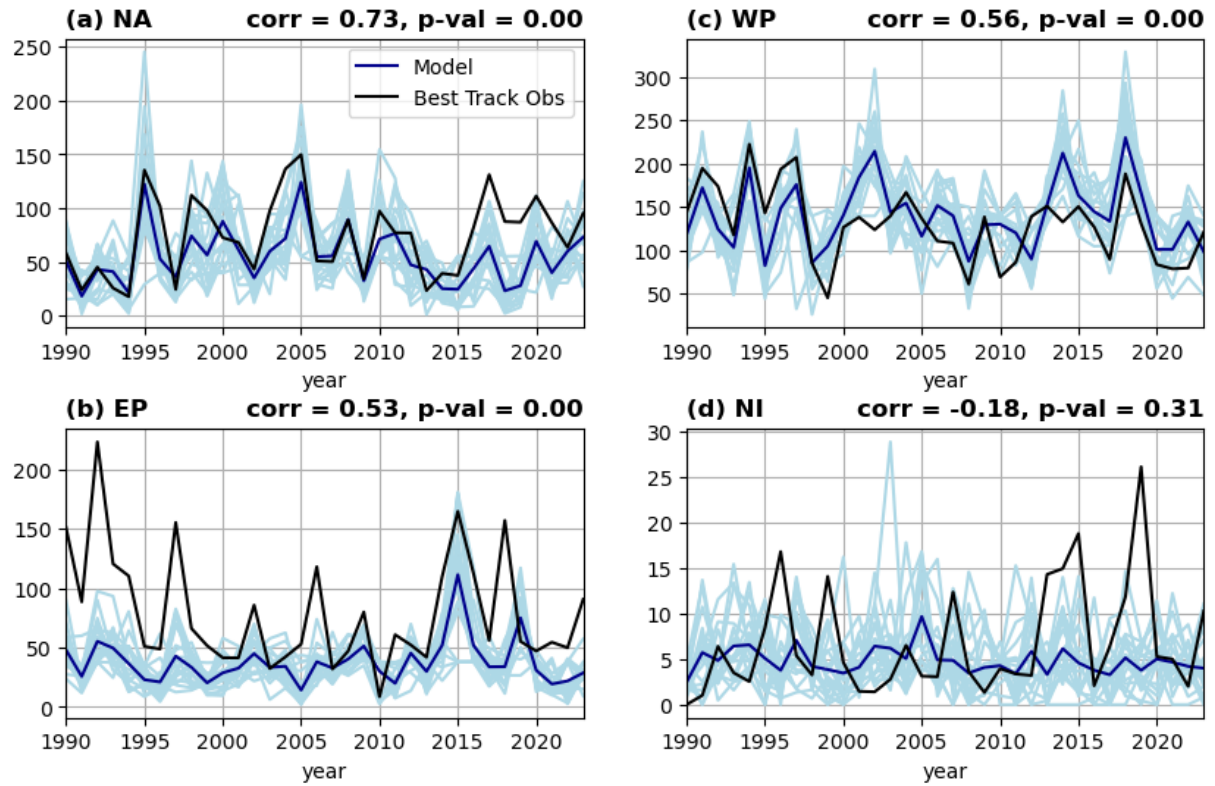
Supplementary Figure 16 *The correlations between the cell counts of TC tracks in the NeuralGCM hindcast and the best track observation. (a) Hindcasts with deterministic physics. (b) Hindcasts with stochastic physics. The counts are calculated based on a 5-degree grid. The dashed contours highlight the correlation coefficients at the 90% confidence level.*



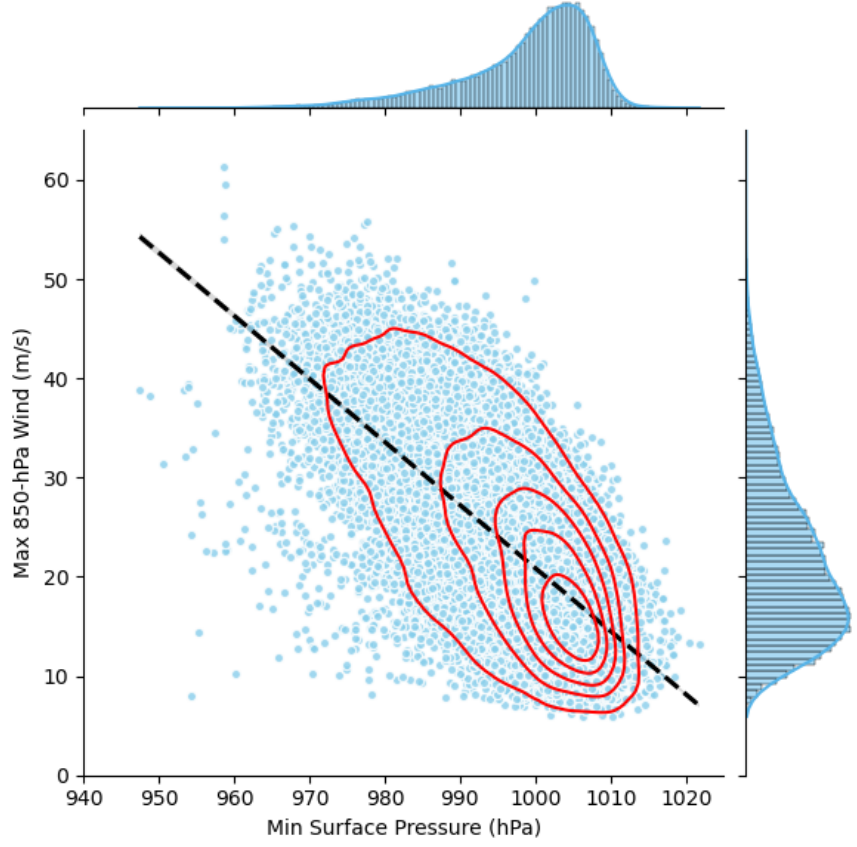
Supplementary Figure 17 *Predictions and observations of the basin-wide TC counts (1990-2023) using the NeuralGCM with stochastic model physics. The other settings are identical to Figure 4.*



Supplementary Figure 18 *Predictions and observations of the accumulated cyclone energy (ACE) using NeuralGCM with deterministic model physics. The ACE is defined as the sum of the squares of the maximum wind speed (knots) of all the available track data. The ACE has been divided by 10,000 for the clarity of the y-axis. The other settings are the same as in Figure 4.*



Supplementary Figure 19 *Predictions and observations of the accumulated cyclone energy (ACE) using the NeuralGCM with stochastic model physics. The ACE is defined as the sum of the squares of the maximum wind speed (knots) of all the available track data. The ACE has been divided by 10,000 for the clarity of the y-axis. The other settings are the same as in Figure 4.*



*Supplementary Figure 20 (a)* The relationship between the surface pressure (hPa) and the 850-hPa maximum wind speed ( $m s^{-1}$ ) in the NeuralGCM hindcasts with the deterministic model physics. The blue dots show the individual data points. The red contours show the kernel density estimate of samples. The histograms on the right and the top show the distributions of the maximum 850-hPa wind speed and the minimum surface pressure. The surface pressure and wind speed of TCs are inversely correlated.

*Supplementary Table 1 Correlation of basin-wide TC frequency between seasonal predictions and the best track observations. The NeuralGCM results contain two rows that represent the hindcasts with the deterministic version (top) and the hindcasts with the stochastic version (bottom), respectively. The value ranges of NeuralGCM indicate 95%-confidence level intervals estimated using resampling with replacement. Except for the smaller number of resampling runs ( $N=1000$ ), the other settings of the skill estimation are similar to those in Zhang et al. (2019). The ensemble size and evaluation period are consistent between studies so the comparisons are relatively fair.*

Reference and Evaluation Configuration	Model	N Atlantic	NE Pacific	NW Pacific
<b>Chen and Lin (2013)</b> <b>5-member ensemble</b> <b>1990–2010</b>	HiRAM	0.88	0.61	0.34
	NeuralGCM	0.74–0.87 0.69–0.88	0.54–0.73 0.37–0.71	0.19–0.46 0.04–0.37
<b>Zhang et al. (2019)</b> <b>12-member ensemble</b> <b>1981–2014</b>	FLOR	0.60–0.75	0.47–0.60	0.27–0.44
	NeuralGCM	0.68–0.77 0.63–0.77	0.53–0.65 0.41–0.61	0.10–0.30 0.01–0.18